JGR Oceans

RESEARCH ARTICLE
10.1029/2020JC016433

Key Points:
- The strongest geoid height changes are associated with regionally pronounced seasonal signals and secular trends
- In the Subpolar North Atlantic the geoid height trend biases circulation trend estimates based on altimetry
- Altimetry data need correction for geoid height change when long-term variations in ocean dynamics are studied

Correspondence to:
F. Siegismund,
frank.siegismund@tum.de

Citation:
Siegismund, F., Köhl, A., Rummel, R., & Stammer, D. (2020). Temporal variations of the marine geoid. *Journal of Geophysical Research: Oceans*, *125*, e2020JC016433. https://doi.org/10.1029/2020JC016433

Received 20 MAY 2020
Accepted 19 OCT 2020
Accepted article online 31 OCT 2020

©2020. The Authors.
This is an open access article under the terms of the Creative Commons Attribution-NonCommercial-NoDerivs License, which permits use and distribution in any medium, provided the original work is properly cited, the use is non-commercial and no modifications or adaptations are made.

Temporal Variations of the Marine Geoid

F. Siegismund[1,2], A. Köhl[1], R. Rummel[2], and D. Stammer[1]

[1]Institute of Oceanography, Center for Earth System Research and Sustainability, University of Hamburg, Hamburg, Germany, [2]Institute for Astronomical and Physical Geodesy, Technical University of Munich, Munich, Germany

Abstract The effects of temporal changes in the marine geoid on estimates of the ocean dynamic topography are being investigated. Influences from mass redistribution due to changes of land hydrology, ice sheets, glacial isostatic adjustment (GIA), and ocean and atmospheric dynamics are considered, and the associated crustal deformation is included. The strongest signals are associated with the seasonal cycle caused by changes in terrestrial water storage and ice sheets as well as the redistribution of atmospheric mass. Second to this is the importance of an overall trend caused by GIA and decreasing ice sheets over Greenland and Antarctica. On long spatial scales, the amplitude of regional trends estimated for the geoid height has a sizable fraction of those from sea level anomaly (SLA) for the period 1993–2016, also after subtraction of steric height of the upper 1,000 m to analyze trends in deep ocean geostrophic currents. The estimated strong negative geoid height trend south of Greenland for the period 1993–2016 opposes changes in dynamic sea level for the same period thereby affecting past studies on changes of both the strength of the subpolar gyre based on SLA and the meridional overturning circulation on a section between Cape Farewell and Portugal applying ocean dynamic topography and hydrography. We conclude that temporal geoid height trends should be considered in studies of (multi)decadal trends in sea level and circulation on large spatial scales based on altimetry data referenced to a geoid field.

Plain Language Summary Changes in ocean surface currents are routinely obtained from satellite altimetry data. A correction for changes in the geoid, the equipotential surface of gravity closest to sea level, is considered small and thus usually neglected. We investigate temporal geoid height changes and potential implications on ocean circulation studies using space-borne gravity data and results from ocean and atmosphere models to discover the individual processes of mass redistribution in the climate system causing thereby changes in the geoid height. We found the largest signals in the seasonal cycle for terrestrial hydrology in the Amazone basin and in negative trends for the Greenland and West Antarctic Ice sheets. For the period 1993–2016 and on spatial scale larger than 1,000 km or so the magnitude of the negative marine geoid height trend south of Greenland is similar to the strength of the negative trend in geocentric sea level from altimetry. This outcome affects past studies on changes in the strength of the subpolar gyre and the Atlantic meridional overturning circulation that neglect geoid height variations. We conclude that temporal geoid height trends should be considered in studies of (multi)decadal trends in sea level and circulation on large spatial scales based on altimetry data.

1. Introduction

In oceanography the marine geoid represents an important reference surface relative to which the ocean dynamic topography (ODT) can be inferred from sea surface height (SSH) measurements obtained by satellite altimetry. In the past temporal variations of the geoid were presumed to be small compared to other error sources and were neglected. Under this assumption, any difference from the underlying geoid model of the SSH field as measured, for example, by an altimeter, would only result from a moving ocean (neglecting any atmospheric contributions).

Over the last decades much effort was devoted by the geodetic and oceanographic community to obtain detailed knowledge about the shape of the geocentric sea surface relative to the marine geoid down to 100-km spatial scale so as to allow a continuous monitoring of ocean geostrophic surface currents from space. After considerable advances in technologic and scientific devotion, the geometry of the sea surface is now measured routinely by satellite altimetry with a remarkable precision of the order of 1 cm over a

horizontal scale of 100 km. Equally remarkable progress has also been achieved in improving geoid models, especially through modern precise space-borne gravity field observations obtained by the U.S./German satellite Gravity Recovery and Climate Experiment (GRACE; Tapley et al., 2004, 2019) and the ESA GOCE (Rummel et al., 2002) satellite missions. Both developments together now allow to compute accurate absolute dynamic surface topography slopes and from this geostrophic surface current on horizontal scales down to about 100 km with an accuracy of 5 cm/s in midlatitudes (Bruinsma et al., 2014).

With its high precision, the GRACE observations also impressively documented broadband (in time) geoid variations associated with mass movements within the Earth and climate system, involving all climate components. Causes for those movements are manifold, ranging from changes in the ocean and atmospheric circulations, changes in the terrestrial hydrology, to changes in the cryosphere and especially melting polar ice sheets and changes of mass distribution in the solid Earth due to, for example, tectonics, glacial isostatic adjustment (GIA), and earthquakes.

In the past, temporal geoid variations were usually neglected while deriving SLA and temporal mean dynamic topography (MDT) from satellite data. However, already in the years leading to the GRACE mission the geoid effect of atmospheric masses and mass movements was discussed at length in the literature (Christodoulidis, 1979; Ecker & Mittermayer, 1969; Rummel & Rapp, 1976). In preparation of the GRACE mission several studies were therefore carried out to estimate the geoid effect of mass changes in the Earth system (Chao, 2003; Dickey et al., 1997; Wahr et al., 1998). If neglected while deriving the ODT, this can cause problems as it would lead to distorted dynamical sea surface slope estimates and thus distorted ocean currents. Since the sea surface shape adjusts quasi-instantaneously to the time-varying geoid, neglecting temporal geoid changes would project all geoid changes directly into the ocean ODT. However, details of the resulting uncertainty in space-based geostrophic velocity observations were never quantified.

With recent progress about geoid changes and their amplitude, it is now timely to rethink the concept of computing sea surface currents from the difference between time-varying altimetry and static geoid models. Most of past studies dealing with temporal gravity field changes were dedicated to the detection and analysis of the associated mass redistribution in the climate system. For the ocean this applies specifically to investigations of sea level and regional ocean mass change (see, e.g., Tapley et al., 2019, and references therein). Though implicit to those studies only few publications address temporal geoid height variations over the ocean. As an example, studies in the pre-GRACE (Nerem et al., 2000; Wahr et al., 1998) and early GRACE period (Moore et al., 2005, 2006) infer mass redistributions in the Earth climate system from observed changes in gravity. Frederikse et al. (2017) consider geoid height changes in the Northwest Atlantic.

A number of recent publications deal with self-attraction and loading (SAL) effects caused by the coupled process of mass redistribution, crustal deformation, and change in gravity (Tamisiea et al., 2010; Vinogradova et al., 2010, 2011). These publications investigate effects on relative sea level and ocean bottom pressure (OBP). Results from these studies support the analysis of observations from tide gauges and bottom pressure sensors, especially if comparing to ocean circulation models, since those usually do not include temporal changes neither in topography nor the geoid. Variations in the geoid changes, though implicit in these studies, were not considered explicitly. The Gauss-Listing geopotential value W_0 temporal variability is discussed in Dayoub et al. (2012), while we here concentrate on geoid gradients. We refer to Wahr et al. (1998) as a prominent example of the latter category.

In this paper, we revisit the question of what causes the geoid to vary as function of time scales to address three questions:

1. What kind of mass redistributions in the climate system are the main contributors to ocean geoid variations for time scales from weeks to decades;
2. How large are geoid height changes arising from mass variations associated with the ocean and atmospheric circulations as a function of geographic position, specifically: Do they matter (for specific time scales) compared to terrestrial signals; and
3. Do we need to account for temporal geoid changes in oceanographic applications?

The goal is to find the dominant contributions to ocean geoid height change for different time scales from weeks to decades and to address the geophysical processes involved. The focus is here on significance of geoid height changes for possible impact on ocean circulation studies. While the overall variations in geoid height are obtained from a state-of-the-art GRACE Level 3 product, additionally, the contributing

effects associated with ocean and atmospheric circulation are investigated separately. This is done to separate contributions from overlapping components of the Earth system. More specifically, contributions from atmospheric circulation are separated either from those of the terrestrial system or the ocean circulation.

The spatial resolution of geoid height changes available from GRACE products is considered sufficient for our study, though the application of dynamic modeling would allow higher resolution for changes associated with ocean and atmosphere circulation. However, since the geoid height change is proportional to the spatial scale of the associated mass change (see Equations 4–6 below), the sensitivity to small-scale mass changes is low and the magnitude of geoid height variations diminishes with decreasing scale. In addition, on short spatial scales rather large variability in SSH is observed from altimetry caused by mesoscale eddy activity. Thus, no significant impact of geoid height changes onto oceanographic applications is expected on these scales.

Our study considers geoid variations arising from (i) water mass cycling between the Earth system components, including terrestrial water storage (TWS), formation and melting of ice, global atmosphere and ocean mass, (ii) the atmospheric dynamics, (iii) the ocean dynamics, and (iv) GIA. Post-Little-Ice-Age adjustment processes, earthquakes, and long-term mantle-core processes also lead to changes in the marine geoid. However, their effect is neglected here. Respective unaccounted temporal geoid variations might cause errors on all time scales, specifically the annual cycle due to cycling of water mass through all components of the Earth climate system. GIA and the mass redistribution associated with nonsteric global sea level rise might cause considerable trends in the geoid.

The structure of the remaining paper is as follows: Section 2 introduces the data sets and the methodology used. For TWS and ice mass changes state-of-the-art GRACE solutions are applied, and no further validation is provided here. For geoid changes caused by atmospheric and ocean dynamics, however, we compare with external data in section 3. Net geoid variations observed over the period 2003 through 2012 are described in section 4. These variations are then split into fast (section 5) and seasonal variations (section 6) and linear trends (section 7). In section 8, the observed geoid trends are compared to trends in (sterically corrected) SLA from altimetry to discuss the potential impact of neglecting geoid height trends when studying long-term changes of surface (deep ocean) currents. Concluding remarks are provided in section 9.

2. Methodology and Approach

2.1. Components of Temporal Geoid Variations

Temporal geoid variations are usually inferred from a series of states of various static geoid models typically inverted over 1-month periods. Changes between these states represent temporal geoid variations, $\Delta N(t)$, resulting from various mass changes in the Earth system occurring on time scales longer than a month. Shorter-time scale variations need to be accounted for during the inversion process to not be aliased. See Dahle et al. (2013) for details on the generation of time-varying GRACE geoid models.

For our purposes we subdivide the change $\Delta N(t)$ between these geoid states into the following contributions:

$$\Delta N = \Delta N^{dyn}_{atmos} + \Delta N^{dyn}_{ocean} + \Delta N_{comp} + \Delta N_{GIA}. \quad (1)$$

Here, ΔN^{dyn}_{atmos} and ΔN^{dyn}_{ocean} are the contribution of air mass and ocean mass redistribution due to atmosphere and ocean dynamic, respectively while total—globally averaged—mass variations are not considered.

The remaining geoid changes

$$\Delta N_{comp} = \Delta N^{gl}_{atmos} + \Delta N^{gl}_{ocean} + \Delta N_{hydro} + \Delta N_{ice} \quad (2)$$

originate from mass fluxes between the different components of the Earth system by specifying the total mass change in the different terms, namely, variations in TWS (ΔN_{hydro}), land ice mass changes, including glaciers, ice caps, and the Greenland and Antarctic ice sheets (ΔN_{ice}), and total changes in atmospheric (ΔN^{gl}_{atmos}) and ocean mass (ΔN^{gl}_{ocean}). ΔN_{GIA} represents the contribution of glacial isostatic adjustment to the total geoid variations.

For each of the above contributions, crustal deformation due to loading and its effect on the geoid is also considered. However, the dynamic models used to compute ΔN^{dyn}_{ocean} and ΔN^{dyn}_{atmos} assume both the geoid and the topography not to vary with time; thus, water and air mass redistribution due to variations in the geoid or crustal deformation due to loading effects are not considered.

The models applied to identify the various contributions to geoid variations provide mass (re)distribution in form of bottom pressure BP or equivalent water height (EWH), with $EWH = \Delta\sigma/\rho_w = BP/g/\rho_w$, where $= \Delta\sigma$ is horizontal mass density change, gravity acceleration $g = 9.81\,\mathrm{m\,s^{-1}}$, and sea water density $\rho_w = 1{,}028\,\mathrm{kg\,m^{-3}}$. Besides the changes in the geoid, we also show the corresponding variations in EWH where we found that it supports the understanding of the physical processes behind the mass redistribution.

To obtain geoid height changes caused by mass redistribution near the Earth's surface, we follow the methodology described in Wahr et al. (1998). Especially, we apply the standard practice of a thin shell approximation assuming all mass changes at a fixed distance a from the center of the Earth. With this simplification the change in geoid height ΔN is described as a scale-dependent weighting of the corresponding horizontal mass density change $\Delta\sigma$. To apply the weighting, first, the spatial mass change distribution is analyzed to obtain changes in the spectral harmonic (SH) coefficients Δc_{lm} and Δs_{lm} for degree l and order m as

$$\begin{Bmatrix} \Delta c_{lm} \\ \Delta s_{lm} \end{Bmatrix} = \frac{1}{4\pi a} \int_0^{2\pi} d\Phi \int_0^{\pi} \sin\Theta \, \mathrm{d}\Theta \; \Delta\sigma(\Theta,\Phi) P_l^m(cos\Theta) \begin{Bmatrix} \cos(m\Phi) \\ \sin(m\Phi) \end{Bmatrix}, \tag{3}$$

where P_l^m are the normalized associated Legendre functions (see, e.g., Hofmann-Wellenhof & Moritz, 2006) and Θ and Φ are colatitude and eastern longitude, respectively.

Second, the SH coefficients are transformed back to physical space to obtain the change in geoid height as

$$\Delta N(\Theta,\Phi) = a \sum_{l=0}^{\infty} w_l \sum_{m=0}^{l} P_l^m(cos\Theta) \times (\Delta c_{lm} \cos(m\Phi) + \Delta s_{lm} \sin(m\Phi)) \tag{4}$$

applying the degree-dependent weighting

$$w_l = \frac{3\rho_w}{\rho_{ave}} \frac{1+k_l}{2l+1}, \tag{5}$$

with ρ_{ave} the average density of the Earth ($= 5{,}517\,\mathrm{kg\,m^{-3}}$). The Love numbers k_l are taken from Table 1 in Wahr et al. (1998). For degrees l not listed there, linear interpolation between neighboring values is applied. The SH coefficients of horizontal mass density change (Δc_{lm}, Δs_{lm}) transform to the fully normalized SH coefficients of ΔN (ΔC_{lm}, ΔS_{lm}) as

$$\begin{Bmatrix} \Delta C_{lm} \\ \Delta S_{lm} \end{Bmatrix} = \frac{3}{2l+1}(1+k_l) \begin{Bmatrix} \Delta c_{lm} \\ \Delta s_{lm} \end{Bmatrix}. \tag{6}$$

The weighting w_l describes how, depending on spatial scale, a mass density change (and thus also EWH) transforms into geoid height change. Since the weighting is reciprocal to spherical harmonic degree, the geoid height is more sensitive to mass changes on large spatial scales. For hemispheric (degree one) mass redistribution the geoid height change will be roughly 20% of the corresponding change in EWH. For degree 100 (200 km spatial scale) the geoid height change is, however, just 2.7% of the mass change.

2.2. Estimating Geoid Variations by Component

For temporal geoid variations on land, both from hydrological processes and the cryosphere, we apply one of the available Level 3 gridded land field products based on space-borne observations of the GRACE. Estimates of atmospheric mass changes and GIA are already subtracted in those data sets, so that they come as adequate and ready-to-use products for our purpose. Over the ocean and for atmospheric mass change over land, we apply results from dynamical models. This allows for higher temporal resolution than available from GRACE; leakage of strong land signals into the ocean is avoided, and a separation of ocean and atmospheric signals is provided.

In the following subsections we will explain the models applied and their application. Because we intend to analyze geoid variations ΔN over the period 2003–2012, all anomalies discussed below will therefore be referenced to this period.

2.2.1. ΔN_{GIA} Estimates

We apply GIA rates for a compressible Earth computed using the ICE5G ice history and the VM2 viscosity profile model (Geruo et al., 2012). It has to be stated that, though post-glacial rebound trends among different GIA models provide robust pattern, the uncertainty of magnitudes in regional trends from different GIA models is rather large (Caron et al., 2018). The total geoid height trend we present here is, however,

independent from the GIA model, since for consistency we have added back the same model that has been subtracted during GRACE processing. This model has been applied to remove GIA rates when producing the JPL Mascon solution we use for geoid height changes from hydrological processes and the cryosphere. Adding this model back is thus indicated to obtain an unbiased estimate of total geoid height change.

2.2.2. $\Delta N_{ice} + \Delta N_{hydro}$ Estimates

For mass changes due to changes in ice including ice caps, glaciers, and the Greenland and Antarctica ice sheets, as well as hydrological changes, we apply the NASA Jet Propulsion Laboratory (JPL)-Mascon solution (Release 5, Version 2 Watkins et al., 2015; Wiese et al., 2015, 2016). From the provided 0.5° resolution the data are binned to a $1° \times 1°$ grid, the resolution we use throughout our study.

2.2.3. ΔN^{dyn}_{ocean} Estimates From GECCO Reanalysis

Geoid variations caused by ocean dynamics are calculated from the GECCO2 reanalysis (Köhl, 2015). As with the atmospheric mass variations we separate ocean mass variations ρ_{ocean} with $\rho_{ocean} = \rho^{dyn}_{ocean} + \rho^{gl}_{ocean}$ into a dynamic and a global mean contribution. The dynamic surface mass density ρ^{dyn}_{ocean} is directly calculated from variations in hydrography and sea level of the dynamic model. Since GECCO2 utilizes the Boussinesq approximation, it is however not capable for producing global mass variations. Instead, global ocean mass changes are calculated from variations in total TWS, the ice mass budget, and global atmospheric mass by claiming the global water mass budget to be closed. As already stated in section 2.1 crustal deformation due to loading is considered in the calculation of geoid changes (Equations 4 and 5), while back coupling of changed bathymetry and geoid to ocean dynamics is neglected.

2.2.4. ΔN^{dyn}_{atmos} Estimates From NCEP Reanalysis

Geoid variations caused by atmospheric mass redistribution are calculated in this study applying daily mean surface pressure from the National Centers for Environmental Prediction (NCEP) and National Center for Atmospheric Research (NCAR) Reanalysis 1 project (Kalnay et al., 1996). We utilize the hydrostatic approximation assuming that changes in surface mass density $\Delta\rho_{atmos}$ are proportional to changes in surface pressure Δp_{atmos}, resulting in $\Delta\rho_{atmos} = 1/g * \Delta p_{atmos}$, with $g = 9.81\ \mathrm{m\,s^{-2}}$ the acceleration of gravity.

Over the ocean, $\Delta\rho_{atmos}$ is spatially averaged to take into account the Inverse Barometer (IB) effect. Due to this effect, regional variations in surface pressure are compensated by inverse variations in sea level so that only the spatial mean variations over the global ocean are detected in the OBP signal, whose variations measure the sum of variations of atmosphere and ocean mass above sea floor. This approach is justified by the long temporal scales considered. For our subsequent analyses the surface pressure is binned to weekly and monthly data sets. Finally, to separate the global mass variations from spatial redistribution, we define $\Delta\rho_{atmos} = \Delta\rho^{dyn}_{atmos} + \Delta\rho^{gl}_{atmos}$, with $\Delta\rho^{gl}_{atmos}$ the global mean of $\Delta\rho_{atmos}$. While $\Delta\rho^{dyn}_{atmos}$ is transformed to ΔN^{dyn}_{atmos} applying Equations 3–5, $\Delta\rho^{gl}_{atmos}$ is transformed to ΔN^{gl}_{atmos} used in Equation 2 to compute ΔN_{comp}.

2.3. Splitting Into Disjunct Frequency Bands

To analyze signal strength and temporal evolution on different time scales, we describe all mass density and geoid height time series as a sum of mutually uncorrelated terms on different frequency bands. Thus, the variances of the different terms add up to the total variance of the time series. For all but the atmospheric component the time series are separated into an annual and monthly mean terms, where the annual mean is defined as anomaly over the reference period (2003–2011) and the monthly mean is defined as anomaly over the year it belongs to. For the atmospheric component in addition high-frequency weekly variations are considered. These are based on daily fields with monthly means subtracted before computing weekly averages.

2.4. Meridional Overturning From Altimetry and Hydrography

In section 8.4 the impact of geoid height changes onto estimates of temporal variations in the meridional overturning circulation (MOC) for a specific section over the North Atlantic is investigated. The magnitude of the upper branch of the MOC is estimated by combining the ODT with upper ocean hydrography information to map pressure on the section and derive geostrophic currents from horizontal pressure differences. Ageostrophic wind-driven transports are computed from wind stress data obtained from the NCEP reanalysis project (Kalnay et al., 1996).

Two different time scales are considered. To investigate the seasonal cycle for each month, the monthly means for each year of the considered period are averaged to obtain climatological values. To focus on interannual and longer time scales, all applied input data are averaged to annual means. The distance between

neighboring grid points on the section is set to 25 km, while the depths are specified by the hydrography data set selected. MDT, SLA, geoid height trend, wind stress, and hydrography maps are interpolated to the grid points on the section, respectively. An additional depth $z = 0$ is defined by applying temperature and salinity of the uppermost level also for the surface. Surface pressure differences are determined from differences in ODT along the section, where the ODT is determined as the sum of MDT, SLA and, when indicated, the geoid height anomaly derived from the trend. With the density defined on the depth levels by the hydrography and expecting linearity of density in-between, the density as well as the pressure is known for arbitrary depths.

The transport for each neighboring grid point pair is then determined as integral from the surface to a selected potential density and accumulated over the entire section. We follow here the approach favored, for example, by Mercier et al. (2015) to define density rather than depth-dependent transports since northward warm waters and southward cold waters reside at overlapping depths and partially cancel each other out when defining depth-dependent transports. The magnitude of the MOC is then defined as the maximum of the (density dependent) transport. To allow for an integration down to a selected potential density and to determine the threshold density of maximum transport, potential density profiles are defined centered between the grid points of the section. Potential density referenced to 1,000-m depth is determined as averages of the potential density profiles of the neighboring grid points. For each pair of neighboring grid points, depth levels for 0.02-kg m^{-3} potential density bins are determined and transports are calculated by integrating down to each of those density levels.

Ekman volume transports are calculated from the wind stress data for each grid point and are expected to evolve linearly between the grid points. Projection perpendicular to the section provides the required transport across the section.

To test the uncertainty of the input data and their impact on the MOC (variations), we apply two different MDT models,

1. The CNES-CLS18 MDT (Rio et al., 2014) and
2. A geodetic MDT based on the GECO (Gilardoni et al., 2016) geoid model and the DTU15 MSS (Andersen et al., 2016). Both, the geoid model and the MSS, are developed until spherical harmonic degree and order 480. The MDT, derived as deviation of the MSS from the geoid, is spatially filtered applying a 0.3° truncated Gaussian filter. The full methodology is explained in Siegismund (2020).

and two different hydrography databases,

1. EN.4.2.1 (Good et al., 2013) and
2. ISAS-15 (Gaillard et al., 2016; Kolodziejczyk et al., 2017)

3. Comparison With GRACE Dealiasing Products

To analyze geoid height changes based on hydrological and ice mass changes, we use a state-of-the-art GRACE product and refer to available validation in the literature (Watkins et al., 2015; Wiese et al., 2015, 2016). For the composite of atmospheric and ocean dynamical components (sum of the first two components in Equation 1), we provide here a comparison with the GRACE Atmosphere-Ocean Dealiasing (AOD) product. The AOD product is based on results from dynamic atmosphere and ocean models and intended to serve as background model for the removal of high-frequency nontidal variability in the production of GRACE level-2 data sets. We use here the version provided by Geoforschungszentrum Potsdam (GFZ; Dobslaw et al., 2013; Flechtner et al., 2015).

We apply here the GAC product, which contains the sum of variations caused by ocean and atmosphere mass redistribution. This product is provided as spherical harmonic potential. The term c_{00}, which contains overall mass change, is not considered, since the atmosphere-ocean composite in Equation 1 considers only mass redistribution with the total mass kept unchanged. After adding the loading effect, the coefficients are transformed to $1° \times 1°$ gridded geoid height anomalies applying the GOCE User Toolbox (GUT).

In Figures 1a and 1b the root mean square (RMS) values of both our ocean-atmosphere composite and the AOD product are shown, respectively. The global means are very close (GFZ AOD and composite: 1.4 mm), the same holds for the spatial patterns. For the region of high variability over Asia our composite shows slightly higher amplitudes than the AOD product. This might be caused by the effect of vertical atmospheric

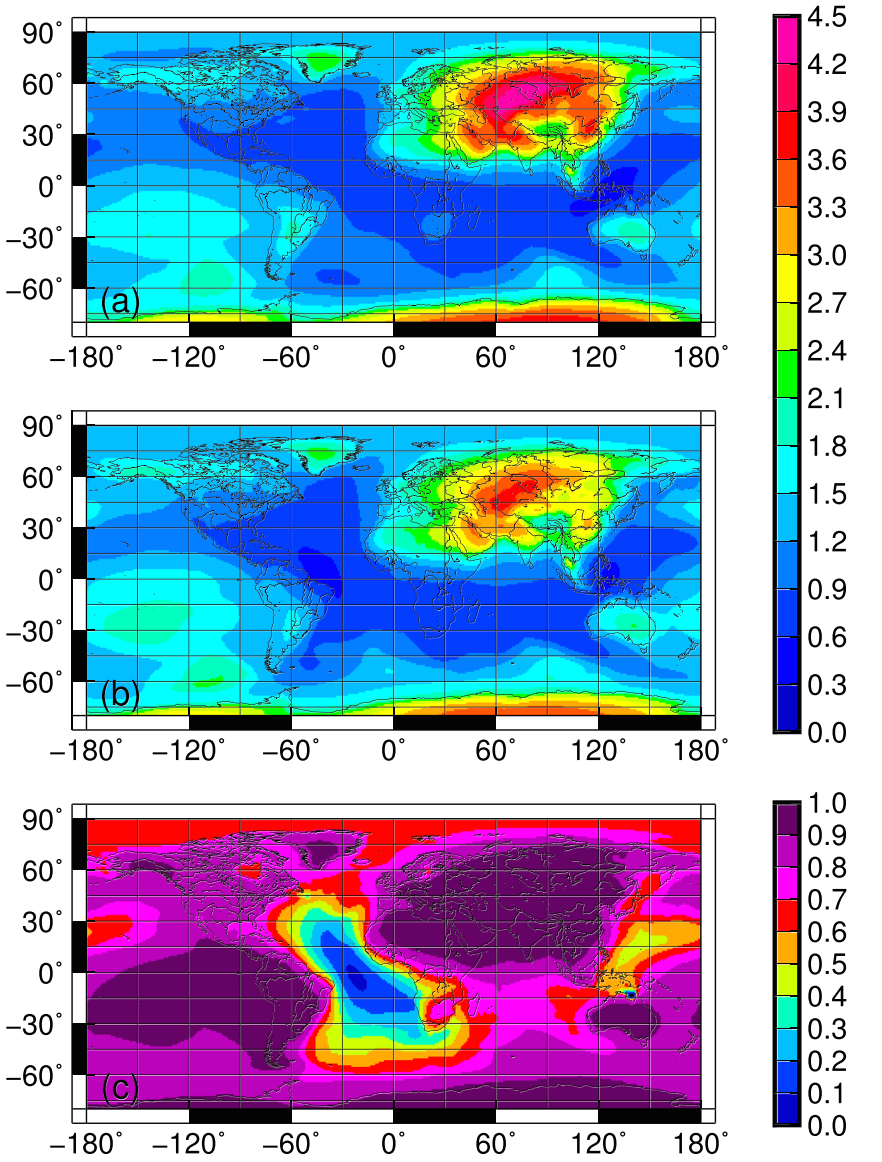

Figure 1. Comparison of geoid changes caused by atmospheric and ocean dynamics ($\Delta N^{dyn}_{atmos} + \Delta N^{dyn}_{ocean}$; see Equation 1) with the GFZ GRACE Atmosphere-Ocean Dealiasing (AOD) product. Displayed are the RMS values (mm) of monthly mean anomalies for (a) $\Delta N^{dyn}_{atmos} + \Delta N^{dyn}_{ocean}$ and (b) the GFZ AOD product; (c) shows the correlation of the two data sets.

mass distribution on the gravitational potential which is taken into account in the AOD product, while in our composite the simple thin shell approximation (according to Wahr et al., 1998) is applied. Figure 1c shows the correlation of the two data sets considered here. While the global average is 0.78, two regions of low correlation are observed: one in the Atlantic and, to a lesser extent, another one in the western Pacific. However, variability in these regions is very low and possible mismatches in geoid height changes are negligible for our study.

4. Net Geoid Variations Between 2003 and 2011

We will start our analysis by quantifying the net geoid variation as obtained from the sum of independent estimates of individual components using Equation 1. The RMS of monthly mean values of this composite is shown in Figure 2a, including all variations on time scales longer than 1 month and shorter than the 9-year-long time series; also included is a trend over the 9-year period resulting from GIA. Enhanced variability can be found over the Amazon basin and especially Greenland and West Antarctica. RMS values

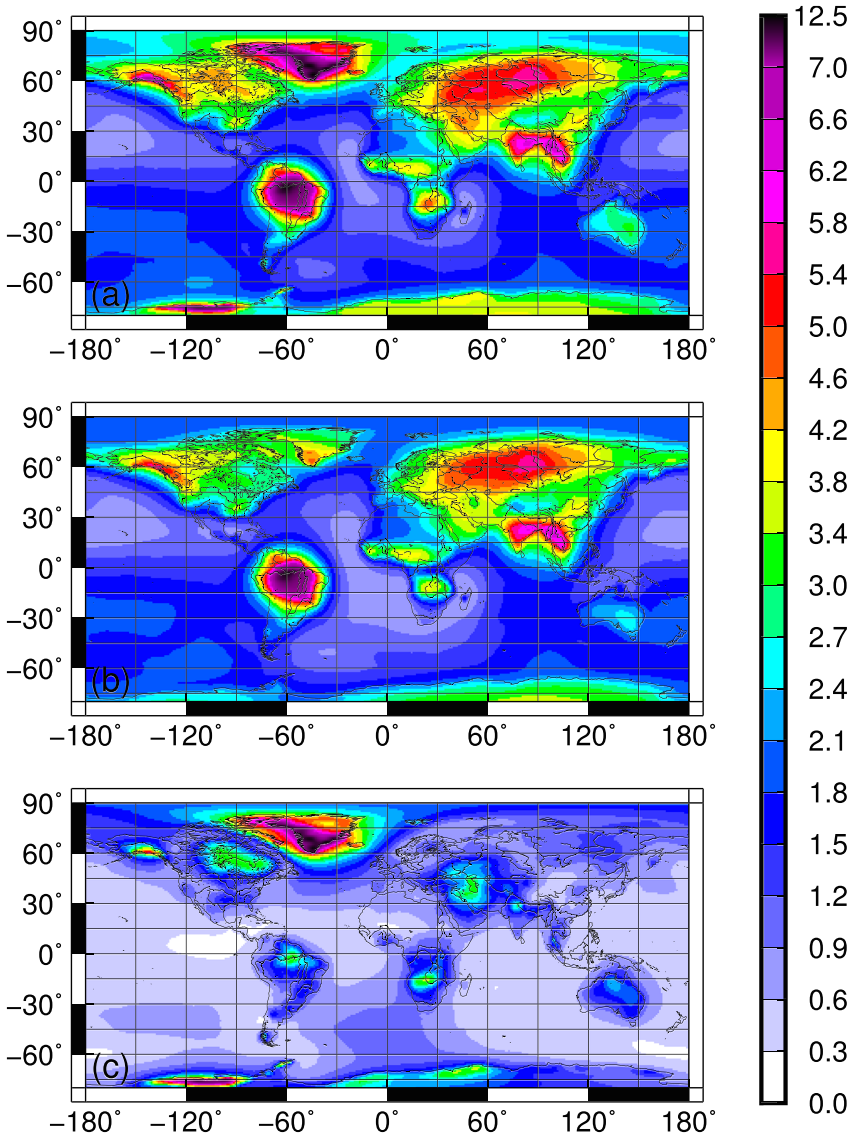

Figure 2. RMS values of geoid variations (mm) based on the composite of individual contributions provided in Equation 1, from (a) unfiltered monthly mean data (2003–2011), (b) monthly mean data with the annual mean subtracted, and (c) annual mean data.

exceed 5 mm also over Siberia, South East Asia, and Alaska. On the monthly to interannual time scales considered here, mass changes in these six regions are the major contributors to ocean geoid changes, while geoid variations over the ocean, away from the dominant sources over land, are relatively small.

Figure 2b shows seasonal and subseasonal variations, while Figure 2c displays interannual and longer time scale variations. A visual comparison of both panels with the top panel reveals that most variations in the original fields reside on the seasonal and subseasonal time scales. On these times scales the largest geoid variations are found over the Amazon basin; smaller amplitude changes are found in Siberia and South East Asia, Alaska and Northwest Canada along the Pacific Coast, over Southwest Greenland, and over Africa. While for Siberia redistribution of atmospheric mass is responsible for the strong signal of approximately 5 mm, for all other regions mentioned we can expect changes in the presence of water mass (either in liquid or in frozen form) to be the primary cause for those changes. In contrast, geoid variations over the ocean are fairly modest, specifically near the equator.

On interannual and longer time scales, enhanced variability or changes can be found over Greenland and West Antarctica associated with the loss of ice masses there on longer time scales; this holds also over Alaska

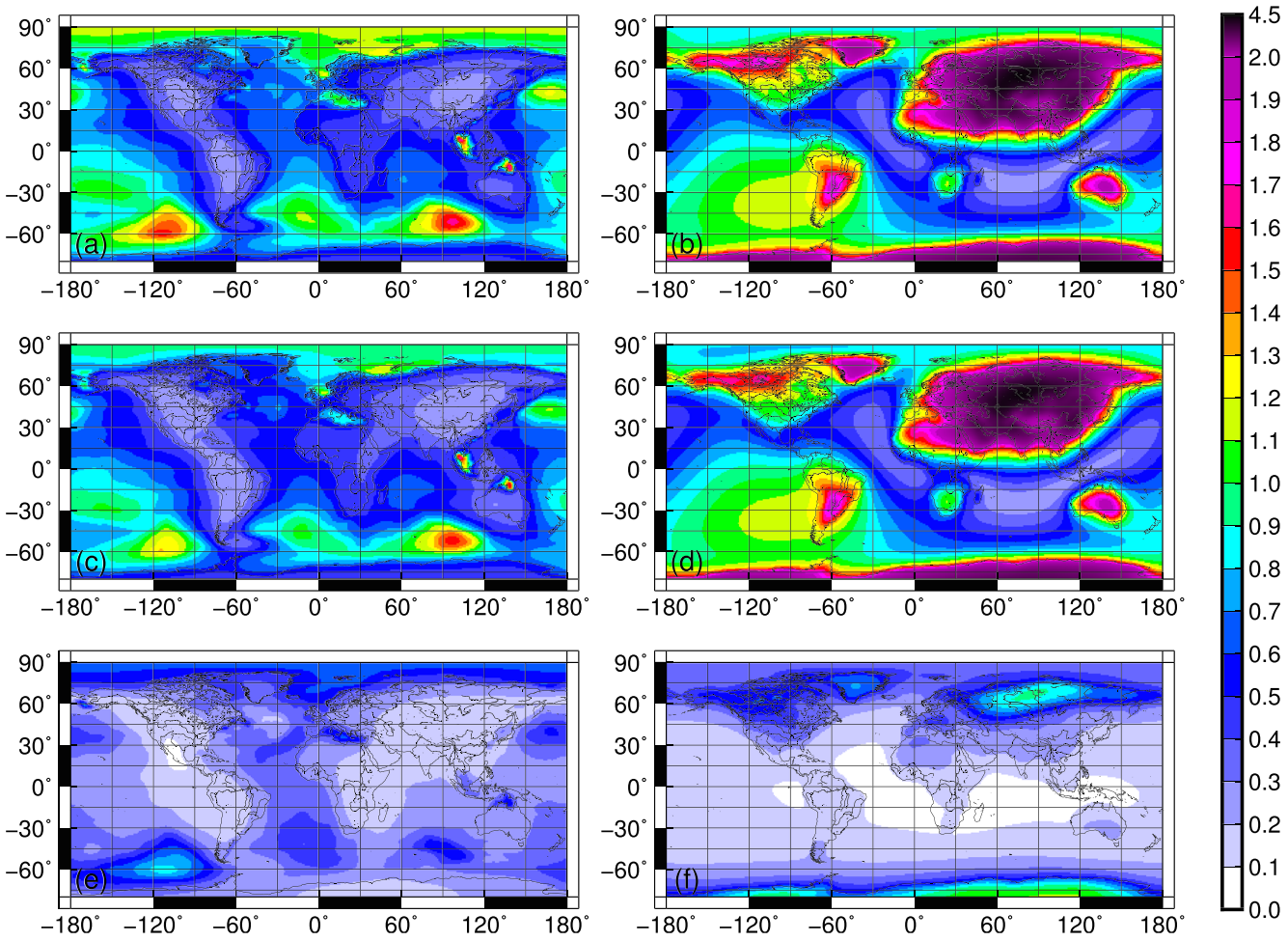

Figure 3. RMS values of geoid variations (mm) from (a, c, e) the ocean dynamic component ΔN^{dyn}_{ocean} and (b, d, f) the atmospheric dynamic component ΔN^{dyn}_{atmos} in Equation 1, from (a, b) unfiltered monthly mean data (2003–2011), (c, d) monthly mean data with the annual mean subtracted, and (e, f) annual mean data.

(probably because of glacial melting Jin et al., 2017). Less prominent signals are found over all continents, for example, between the Black and the Caspian Sea (because of the decline of the sea level in the Caspian Sea Chen et al., 2017), over the Amazon Basin, southern Africa around 15°S, and northeastern Australia.

4.1. Contributions From Atmospheric and Ocean Dynamics

The geoid height changes on monthly and longer time scales, as described by the four contributions of Equation 1, are dominated by ΔN_{comp}, which consists of hydrological processes, mass changes in the cryosphere, and mass fluxes between the different components of the Earth system. We do not present ΔN_{comp} here, which is rather similar to the variations seen in Figure 2 for large part of the globe. Instead, we focus on the remaining components of Equation 1 and want to identify regions and time scales where these components considerably contribute to the net geoid height change presented in Figure 2.

GIA, expressed as a spatially dependent linear trend, is presented in section 7 where interannual changes are discussed. Here we focus on the remaining contributions ΔN^{dyn}_{atmos} and ΔN^{dyn}_{ocean} from atmospheric and ocean dynamics, respectively. The rows in Figure 3 are organized the same way as in Figure 2, with the left (right) column showing the contribution from ocean (atmospheric) dynamics.

(i) Ocean Dynamics: Figure 3a shows the RMS of monthly geoid variations ΔN^{dyn}_{ocean} (mm) caused by ocean dynamics as they result from the GECCO2 ocean state estimate (see section 2.2.2 for details). We recall that variations in global ocean mass are not considered in the figure. The figure reveals enhanced geoid height changes (>1 mm) from ocean mass variations in essentially high-latitude oceans. Most prominent are changes in the Arctic revealing that the mass in this basin is changing substantially on the considered

time scales. Enhanced variability can also be seen in the North Pacific and the Southern Ocean. Some of those locations are known for their enhanced barotropic variability. As an example, Stammer et al. (2000) describe the variability in the Southern Ocean and relate it to high barotropic variability there in the presence of closed f/H contours, with f the Coriolis parameter and H the ocean depth. Mass variations and their contribution to GRACE signal in the North Pacific have been discussed previously by Chambers and Willis (2008). We note here that since we show only variability on monthly and longer time scales, substantial energy is already eliminated since most barotropic changes are on higher frequency.

Most of the RMS variations of monthly variations in ΔN^{dyn}_{ocean} originate from seasonal and subseasonal variations (Figure 3c). Interannual variations (Figure 3e) remain below 1 mm everywhere and are not further discussed here.

(ii) Atmosphere: Shown in Figure 3b is the RMS of monthly geoid variations N^{dyn}_{atmos} caused by atmospheric dynamics related mass fluctuations. The fields were derived from NCEP/NCAR surface pressure fields as describe in section 2.2.3. The surface pressure (not shown) reveals significant variations only over continents, while the (spatially constant) variability over the ocean is with 3.9 mm EWH rather small. Strong variations are observed especially over Asia and also over Greenland and Antarctica. Enhanced atmospheric mass variations but on lower scale can be seen over most of the remaining continents, except the tropical rain forest band.

After conversion to geoid height change (Figure 3b), due to the scale-dependent weighting (see Equations 5 and 6), the continental signals spread over the ocean. Around the Asian continent, RMS of monthly geoid height variations reach 2 mm, and also for Alaska, Greenland, Antarctica, Australia, and part of South America near coastal RMS values above 1 mm are reached. Interestingly, the strong surface pressure variations over Asia produce a significant d/o 1 signal in the corresponding geoid height pattern with a second center of variability in the South Pacific west of Chile. Here RMS values around 1.1 mm are observed. As found in case of the ocean also geoid height changes associated with atmospheric dynamics reside almost entirely in seasonal and subseasonal time scales (Figures 3d), while interannual variations (Figure 3f) remain below 1 mm everywhere and are not further considered.

The analysis of geoid height changes so far should give an overview about temporal variations on intraannual as well as interannual time scales broken down into the contributions of individual Earth climate components and based on monthly mean data. In the following three sections we want to complete this analysis by (i) including fast changes on submonthly time scales and discuss how well the already presented intraannual and interannual variations can be described as a (ii) seasonal cycle and (iii) linear trend, respectively.

5. Geoid Variations on Subseasonal Time Scales

Three individual contributions exist to geoid variations on the submonthly to intraannual time scales, originating from (i) atmospheric mass variations, (ii) fast barotropic oceanic motions, and (iii) terrestial hydrological variations. We note that fast geoid motions on submonthly time scales are not resolved through GRACE monthly fields and thus are not included in Figure 2. Significant submonthly geoid variations might result from atmospheric mass variations. Analysis of NCEP/NCAR weekly surface pressure variations shows that approximately 40% of the variance is made up by submonthly variations. Therefore, we estimated geoid variations caused by atmospheric mass redistribution down to a weekly time scale from external non-GRACE sources as explained in section 2.

This time we show the variations of both mass (Figure 4, left) and associated geoid height (Figure 4, right) to visualize the scale-dependent weighting involved in the transformation process (Equations 5 and 6). The left panel of Figure 4 displays the RMS of surface pressure anomalies associated with air mass redistribution caused by atmospheric dynamics on time scales longer than weekly, after subtraction of the monthly mean. The panel highlights the large pressure fluctuations associated with high-latitude low pressure/storm systems. In contrast, tropical regions are much more "quiet." This holds also in the variations of associated geoid changes shown in the right panel of Figure 4. For regional patterns of strong air mass variability the transformation to geoid height variations both flattens and spreads the signal including larger areas, depending on the spatial scale of the pattern. Especially for Siberia and Antarctica, the large-scale structure of the surface pressure patterns allows the signal to keep substantial magnitude after transformation to geoid height

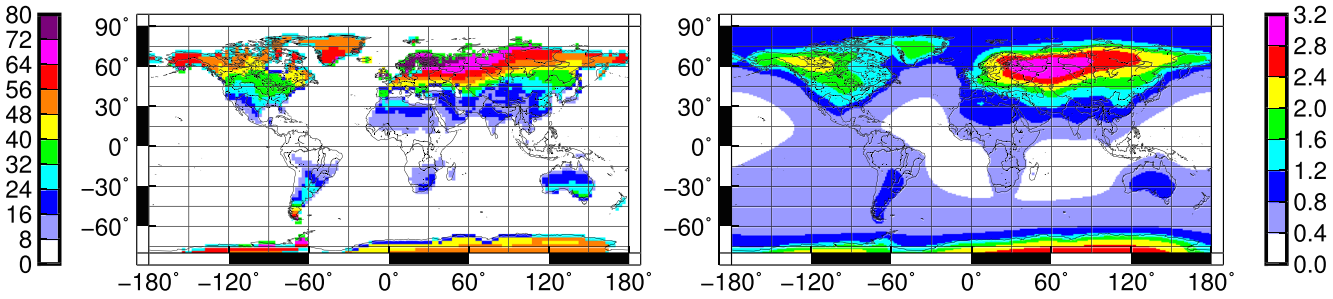

Figure 4. RMS of weekly mean air mass redistribution caused by atmospheric dynamics, after subtraction of the monthly mean. Displayed is the RMS of (left) the surface pressure in terms of equivalent water height (mm) and (right) the geoid height (mm), respectively.

with an RMS of up to 3.2 mm, while the smaller-scale pattern with similar amplitude over Alaska refers to a much weaker geoid height signal. Over the ocean the RMS of geoid height variations exceeds 1 mm only close to Antarctica and in the Arctic Mediterranean.

6. Seasonal Geoid Variations

Since the Earth system shows enhanced variability on the seasonal cycle in many of its components, it can be expected that pronounced geoid variations resulting from associated mass shifts in the system exist on the seasonal cycle.

To isolate seasonal geoid variations from what was shown above in the Figures 2b, 3c, and 3d, we estimated seasonal changes in the geoid by fitting an annual harmonic to our monthly composite of contributions from land ice and terrestrial hydrology, the ocean, and the atmosphere.

Shown in Figures 5b and 5c are the respective amplitude (mm) and day of maximum of the total seasonal geoid variations, respectively. The pattern of amplitudes resembles that of total intraannual variability which we show again in Figure 5a but now with values only over the ocean and the same (but differently scaled) color bar as for Figure 5b for better comparison. The variations over the Amazon, North and Southeast Asia, Alaska, and Southern Greenland are reproduced. Figure 5d displays the percentage of the variance explained by the seasonal cycle relative to the total intraannual variability. Regions with strong variability (Figure 5a) are also those where the variability is explained best so that the bulk of total variability is explained by the seasonal cycle.

Considering ocean dynamics (see Figures 6a, 6c, 6e, and 6g), the seasonal cycle is not as suitable to explain the intraannual variations in mass distribution in contrast to the total or the other components in our composite. Still, the predominant part of the strong variability around Indonesia and east of the Kerguelen Plateau in the Southern Ocean can be attributed to seasonal variations.

For interannual mass redistribution due to atmospheric dynamics (see Figures 6b, 6d, 6f, and 6h), especially those over Asia, the seasonal cycle is a good approximation that explains most of the variability in all regions with strong variability. Over the ocean, the remaining interannual variations in geoid height that cannot be explained by the seasonal cycle are around or below 1 mm.

7. Linear Geoid Trends 2003–2011

As above for the intraannual variations, we checked also if the annual mean variations can be described approximately by a linear trend. Figure 7 displays the results of this test for geoid variations based on the sum of our composite (including GIA). We stated already above that atmospheric and ocean dynamics only play a minor role for interannual geoid height variations. We just note that geoid height trends from ocean (atmospheric) dynamics nowhere exceed 0.3 (0.1) mm a^{-1} (not shown) and that annual mean ocean mass increases around 1.4 mm a^{-1} in terms of barystatic sea level change which is close to what is published recently (e.g., Slangen et al., 2017, and references therein.) Significant geoid height trends are restricted to the cryosphere, terrestrial hydrology, and GIA. We show the total trend in Figure 7, since this is the important parameter for long-term ocean studies, and GIA in Figure 8, since this a significant contribution to the trend.

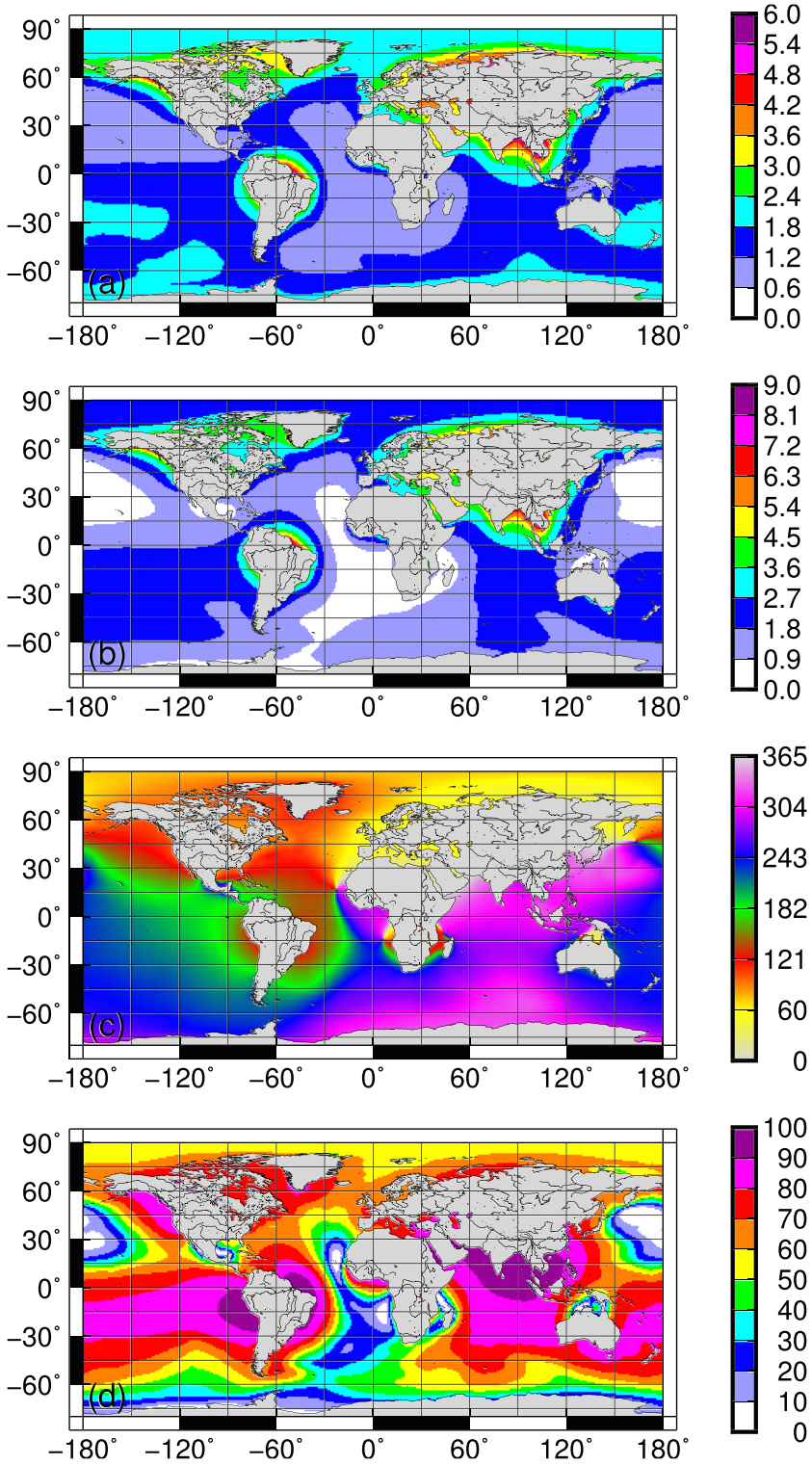

Figure 5. The intraannual variations in monthly mean geoid height based on the composite of individual contributions provided in Equation 2. Results of a least squares fit to a seasonal cycle $A * cos(\omega t - \lambda)$ are presented. Displayed are (a) RMS of intraannual variations (mm) (copy of Figure 2b but now with land masked out and a different color scale), (b) the amplitude A (mm), (c) the day of maximum λ, and (d) the explained variance in %.

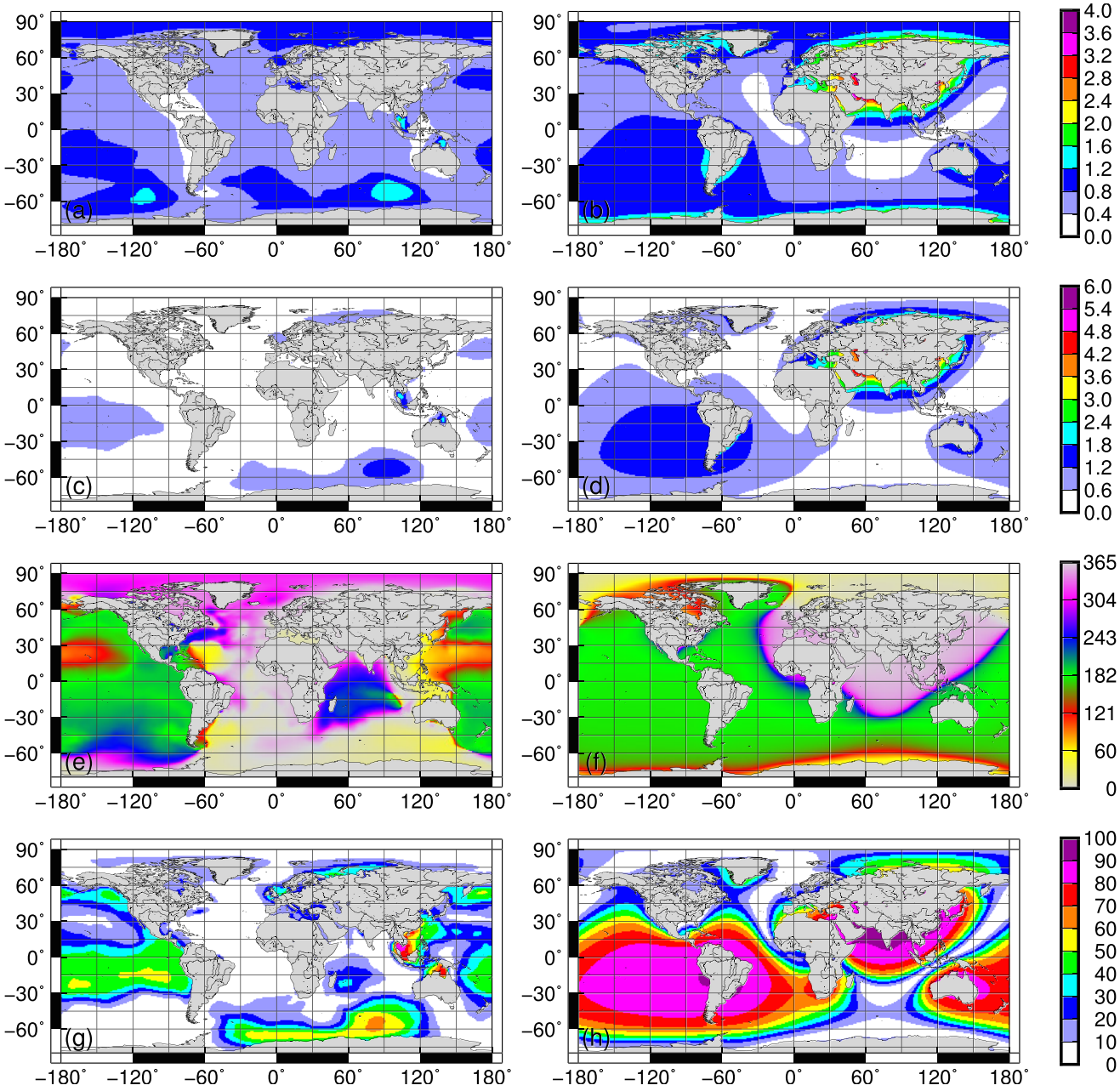

Figure 6. Same as Figure 5 but for water mass redistribution caused by (a, c, e, g) ocean and (b, d, f, h) atmospheric dynamics.

The regionally strong interannual variations around Greenland and parts of Antarctica (see Figure 7a) are predominantly explained by a linear trend (Figure 7b,c). The negative trend south and southwest of Greenland up to more than 7 mm a^{-1} near the coast is by far the largest and thus most important signal for long-term ocean studies.

A very prominent contribution to geoid changes on long time scales is known to originate from GIA. To bring the respective signal into context of the observed linear trend, we show in Figure 8 the geoid height trend (mm a^{-1}) as it is caused by GIA, that is, by viscous mass adjustments in the Earth's mantle. Positive (uplift) signal is centered around the locations of the Laurentide and Fennoscandian ice sheets. Similar signals can be identified over western Antarctica. Centers of respective rebound signals are located in the western subtropical North Atlantic and the southern Indian Ocean. A comparison of Figures 7 and 8 suggests that

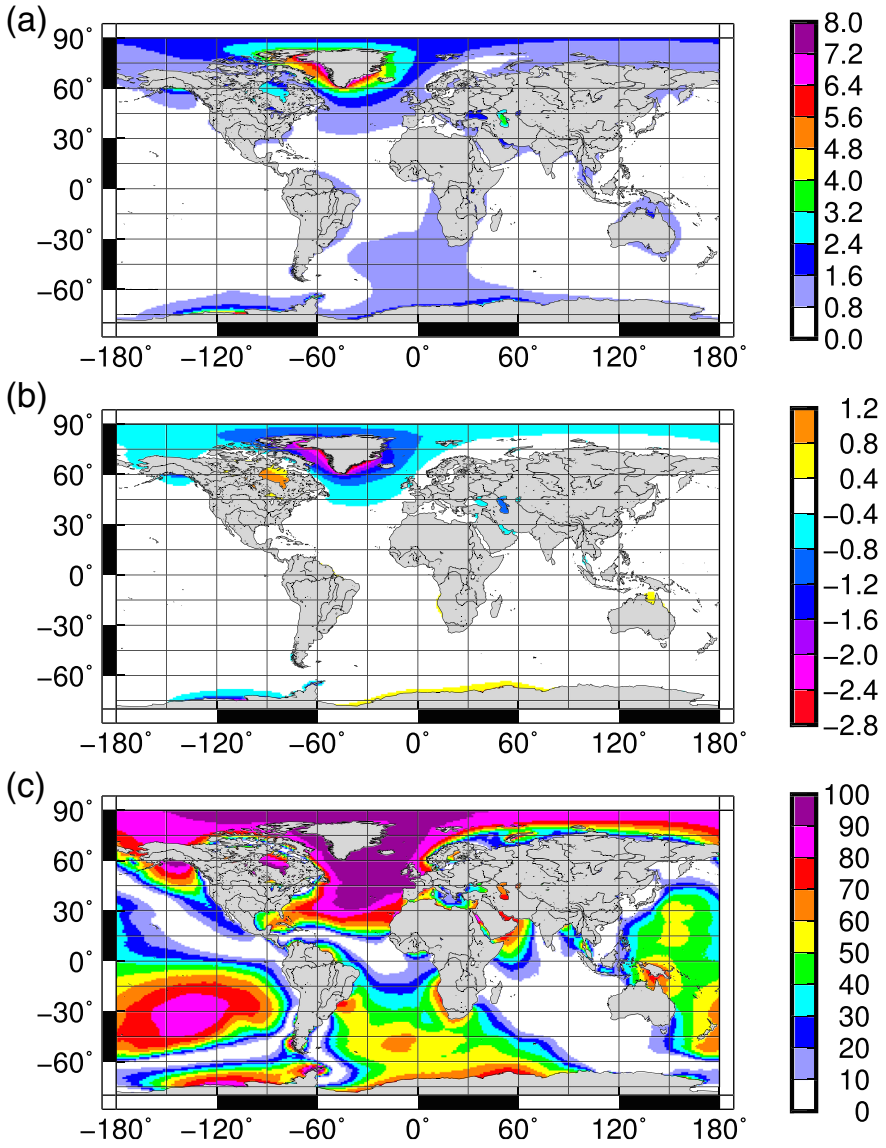

Figure 7. Total geoid height trend (2003–2011) based on the composite of individual contributions provided in Equation 1. Displayed are (a) RMS of interannual variations (mm) (copy of Figure 2c but now with land masked out and a different color scale), (b) the trend (mm a^{-1}), and (c) the explained variance in %.

over the continental North America and northern Europe, the GIA signal is counter balancing the trend caused specifically by changes in the terrestrial hydrological cycle in these regions.

The GIA trends among different GIA models provide robust pattern, but the uncertainty of magnitudes in regional GIA trends from different GIA models is rather large (Caron et al., 2018). Following the supporting information, Figure 4 of Caron et al. (2018), this might be especially true for the negative trend centered in the tropical North Atlantic with uncertainty in the order of 0.1 mm $year^{-1}$.

8. Potential Impact on Dynamic Topography and Transport Estimates

Changes in geoid height are generally ignored when investigating temporal variations in sea level from altimetry data. From the analysis presented above this approach seems justified for short spatial and temporal scales because of considerably larger variability in sea level anomalies from altimetry than of the geoid. However, when discussing interannual and longer-term variations and trends, the observed sea level amplitudes are usually much smaller. When ignoring geoid height variations, the potential bias in sea level variation studies relative to the investigated signal grows with the time scale considered.

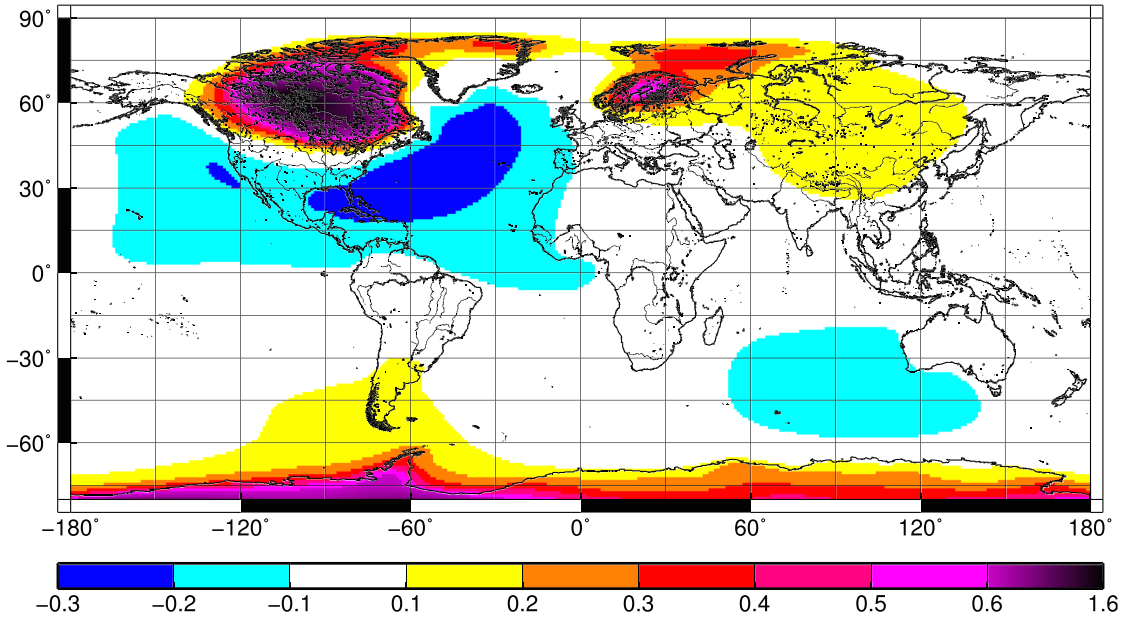

Figure 8. Geoid height trend (mm a^{-1}) caused by postglacial rebound.

In the following subsections we provide three examples for sea level and circulation studies with potentially large impact from geoid height changes on their findings. Due to the massive mass loss of the Greenland ice sheet and in addition a negative GIA trend south of Greenland, the highest long-term geoid changes are found in the North Atlantic. We will therefore focus on this region. In all three cases we investigate the impact of geoid height change by performing two test cases. In the first case geoid height is supposed invariant, while in the second case the geoid height change is considered and subtracted from the altimetry data. The differences of the outcomes are discussed.

8.1. Geoid Height Changes 1993–2018

Since the so far considered period 2003–2011 is rather short to investigate the impact of geoid height changes on long-term variations in sea level and ocean circulation, we apply additional external data to allow for an extension of our composite data set to the period 1993–2018, which then covers almost the entire era of altimetry until today. To do so, we use a recent assessment of changes in the Greenland ice sheet mass balance provided by the Ice sheet Mass Balance Intercomparison Exercise (IMBIE; Team, 2020).

From the monthly IMBIE data set, annual mean scaling factors c_i are calculated for the years 1993–2002 and 2012–2018. c_i are calculated as quotients of annual mean ice mass balance for year i and the mean mass balance for the period 2003–2011. The scaling factors are then used to scale the 2003–2011 mean local mass balances from our composite data set to obtain estimates of local mass balances MB_i for the years i before and after 2003–2011. Application to the full mass signal in the Earth climate system (without GIA), rather than Greenland only, is done here to ensure a closed overall mass budget. This approach causes no major source of error since the Greenland ice melt signal is by far the largest signal of the climate system in the region considered.

A monthly mass climatology is calculated from the composite by averaging for each month over the entire period 2003–2011 of the composite after subtracting the linear trend. Starting from December 2003 (January 2012), the mass balances MB_i are integrated backward (forward) in time and added to the corrected-for-seasonality ice masses of January 2003 (December 2011) to obtain monthly ice masses before 2003 (after 2011). Finally, the monthly climatology is added for both extensions, before 2003 and after 2011, to estimate the seasonal cycle. Finally, after transformation to geoid height anomalies, the GIA trend is added. The temporal development of the Greenland ice mass is obtained from the JPL mascon solution we use in our composite as well as the extensions calculated applying the scaling methodology just described as displayed in Figure 9. For comparison, the respective data set from the IMBIE project is shown as well. The two data sets correspond closely with a slightly higher absolute trend in the JPL Mascon solution. Corrected

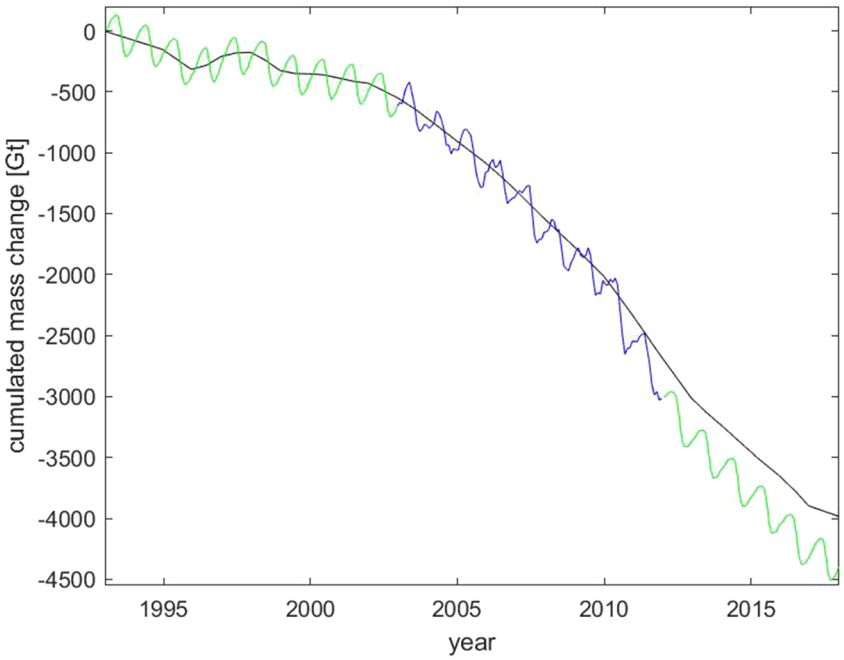

Figure 9. Cumulated Greenland ice mass anomalies (Gt) based on the JPL mascon solution (blue) and IMBIE (black). The green lines represent the extensions of the mascon solution for the periods 1993–2002 and 2012–2018.

for the seasonality, the accumulated difference between the two data sets over the full 1993–2018 period is 479 Gt and somewhat above the uncertainty of 346 Gt specified for the IMBIE data set.

8.2. North Atlantic Subpolar Gyre Strength

A prominent example of analyzing large-scale ocean circulation changes based on altimetry is the strength estimation of the North Atlantic Subpolar Gyre. For this analysis we apply the delayed-time all-satellite merged altimetry data provided by the Copernicus Marine and Environment Monitoring Service (CMEMS) for the period 1993 to 2016. The data are binned to annual means on a $1° \times 1°$ grid. The standard methods to filter out small-scale signals like spatial filtering or spectral methods based on Fourier Transforms or spherical harmonics have the disadvantage to smooth also the patterns of long-term variations we are interested in. Therefore, we use instead an empirical orthogonal function (EOF) analysis here which automatically provides modes with long scales of coherency in the leading EOFs, while local small-scale variations contained in subsequent modes are cut off automatically when using only the leading modes.

The region analyzed (30–65°N, 80°W to 0°E) is identical to the region often used to investigate variations in the strength of the subpolar gyre (SPG; see Hatun & Chafik, 2018, and references therein). The global mean SLA is subtracted to focus on variations in the dynamics which are related to local sea level changes relative to the global mean rather than the global mean itself. We consider two cases: Case (1) applies SLA as described with temporal geoid variations completely included, while in Case (2) SLA is corrected for annual mean geoid height anomalies obtained from our extended composite (see section 8.1). To ensure comparability of the results obtained from the EOF analysis, only the temporal evolution of the modes should differ between the cases while the modes themselves, as described by the EOFs, are identical. Therefore, only one EOF analysis is performed with the time series for the two cases concatenated for each grid point.

We concentrate here on the leading two modes of variability from the EOF analysis. These explain 35% (34%) of the variance in annual mean uncorrected (corrected) SLA, respectively. Hatun and Chafik (2018) argue that these two modes combined are necessary to deduce the strength of the SPG from SLA in recent years, in contrast to the usual description by the (normalized) first PC only, termed as SPG index.

In Figure 10 the results of the EOF analysis are displayed. The PCs carry the units, while the EOFs are normalized. The differences seen in the principal components (PCs) (Figures 10c and 10d) for the two considered cases are predominantly described by a trend over the whole period considered, while interannual time scales are hardly affected. We show these difference in addition to the PCs in Figures 10c and 10d (for

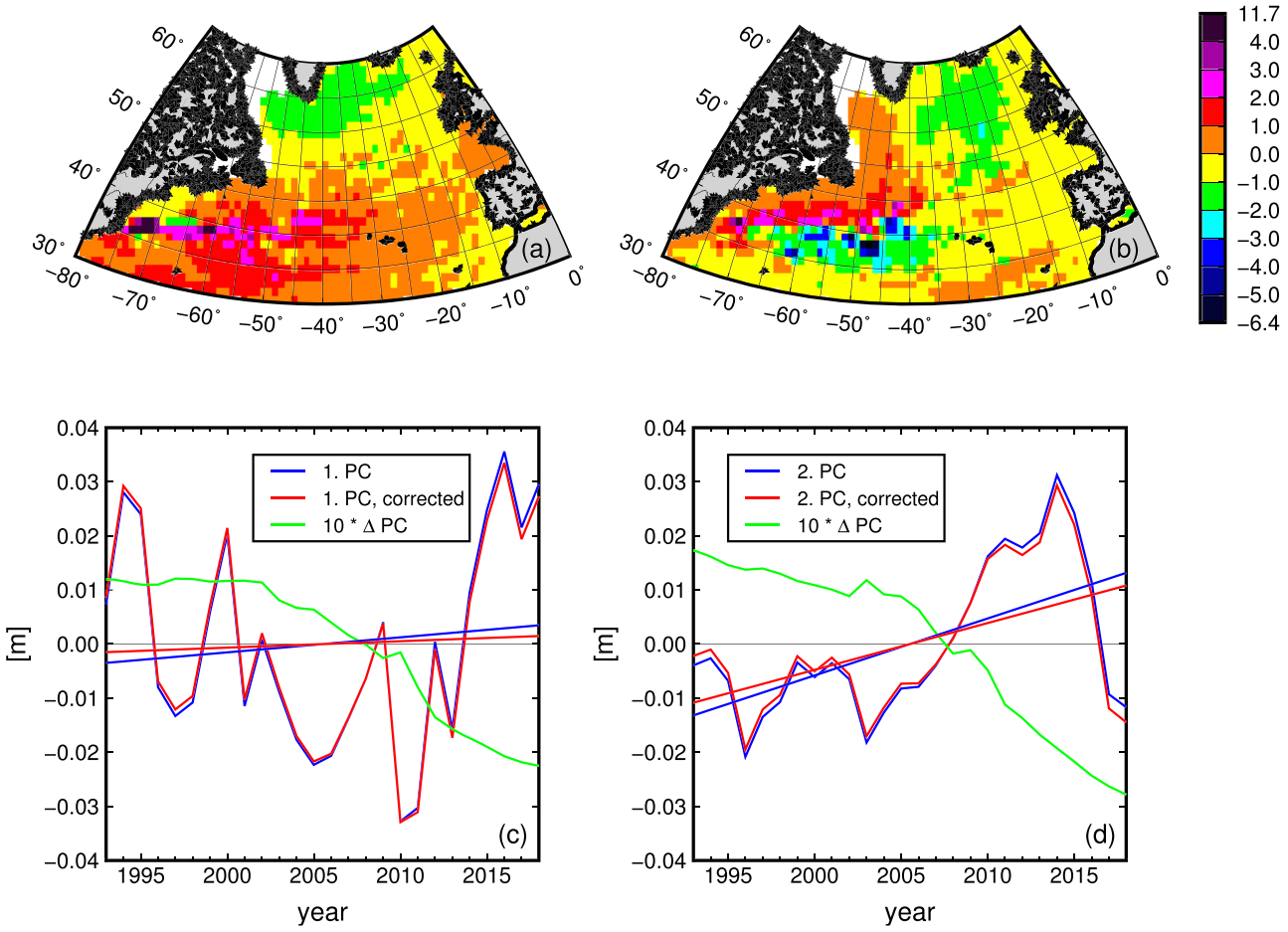

Figure 10. EOF analysis of annual mean SLA from altimetry for the region 30–65°N, 80°W to 0°E. The time series of SLA with and without correction for geoid height change are concatenated to yield common EOFs for the two data sets. Displayed are (a) the first and (b) the second EOF and (c) the first and (d) the second principal component (PC). For the PCs two time series and the corresponding linear trends are provided for the two considered cases: (blue) the SLA is not corrected and (red) the SLA is corrected for geoid height changes. The difference of the time series (corrected-uncorrected case multiplied by 10 is provided as green line.

better visibility multiplied by a factor of 10). From these differences it is clearly seen how the geoid height change south of Greenland projects onto the two leading modes of sea level variability in the subpolar North Atlantic. The trends in the PCs are decreased from 0.28 (1.05) to 0.12 (0.87) mm a^{-1} for the first (second) mode when the SLA is corrected for geoid height changes.

In general, if SLA is not corrected for geoid height change, long-term trend estimates get biased if hydrodynamic processes are investigated and not the change in geocentric sea-level is of interest. This bias will grow with acceleration of melting of the Greenland ice sheet in the future.

8.3. Sterically Corrected Sea Sevel

Temporal changes in sea level observed in altimetry data are an often used indicator for changes in the upper ocean circulation and hydrography. Theoretically, the combination of SLA with density profiles from in situ observations allows a determination of temporal variations in volume, heat, salt transports, and deep ocean circulation. Practically, the spatial and temporal density of temperature and salinity observations has to be sufficient as well as the accuracy of both altimetry and hydrography. The improving knowledge of the regionally dependent upper ocean density profile from ARGO floats in the upper ocean starts to offer an alternative to the standard level of no (or known) motion approach. To determine changes in the weak deep ocean currents, this does, however, also increase the requirements on the accuracy of sea level gradients. We want thus in a second example analyze the potential impact of the usually neglected geoid height change on estimates of changes in the deep ocean circulation based on sterically corrected SLA.

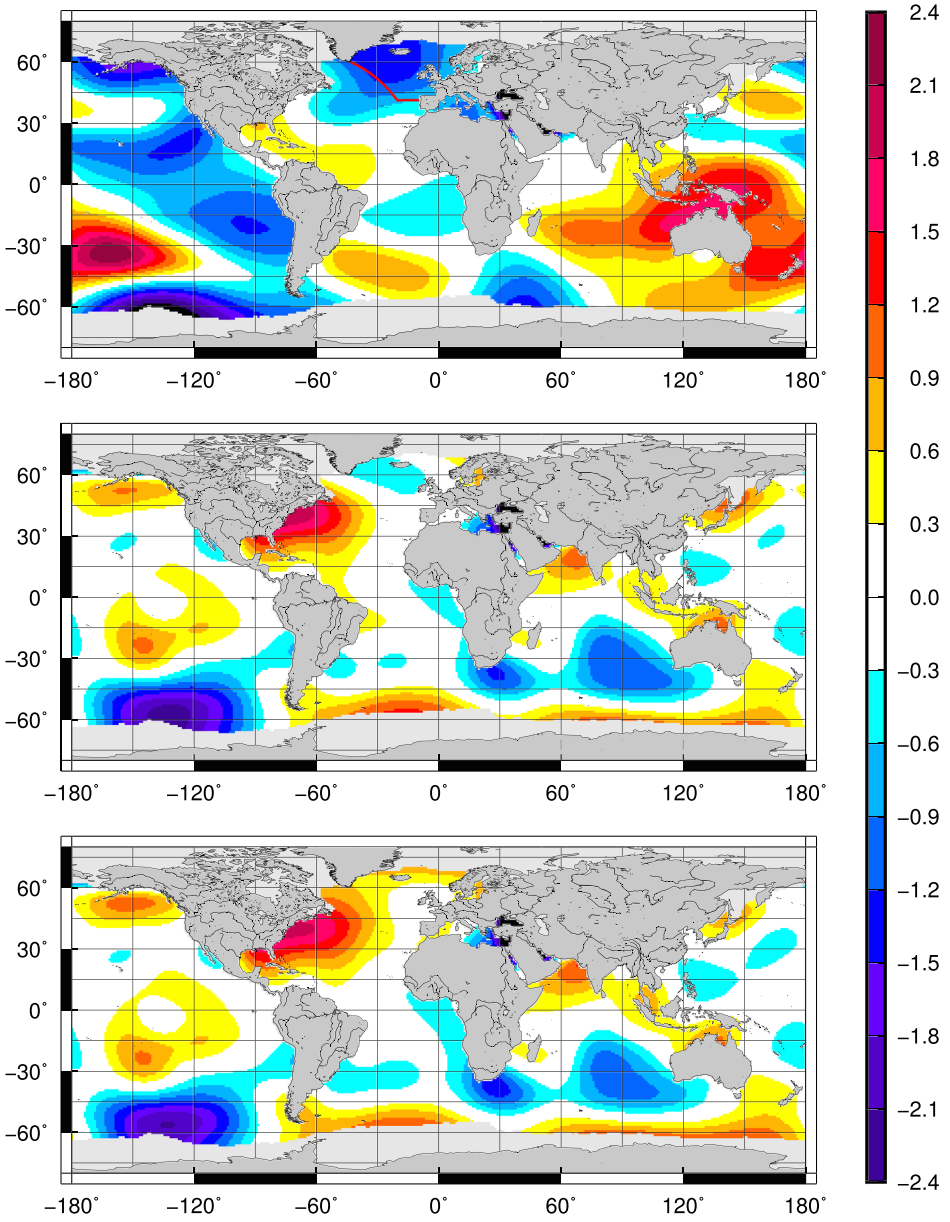

Figure 11. Trend in sea level anomalies from altimetry (1993–2016, mm a^{-1}) after subtraction of (top) the global mean, (middle) in addition the steric height for the upper 1,000 m, and (bottom) in addition the linear trend in geoid height (see section 8.1). In addition, in the top panel the section used for MOC strength estimates in section 8.4 is displayed.

The top panel of Figure 11 shows the linear trend in sea level for the period 1993–2016 after subtraction of the global mean and smoothing the SLA with a 10° spatial Gaussian filter truncated after two standard deviations, a number of trend patterns of both increasing and decreasing sea level emerge, with amplitudes up to approximately 2 mm a^{-1}. This is close to amplitudes we found for the geoid height shown in Figure 7 (top).

In the middle panel of Figure 11 steric height from surface to 1,000-m depth is subtracted from SLA to correct the total dynamic sea level change from the bulk of the steric effects and provide an estimate of the trend in deep circulation as dynamic height at 1,000 m. The trends are now generally smaller near the equator and again in the order of the geoid height trends. This points to a significant influence of geoid trends when altimetry is combined with in situ hydrography to estimate long-term changes in deep ocean circulation.

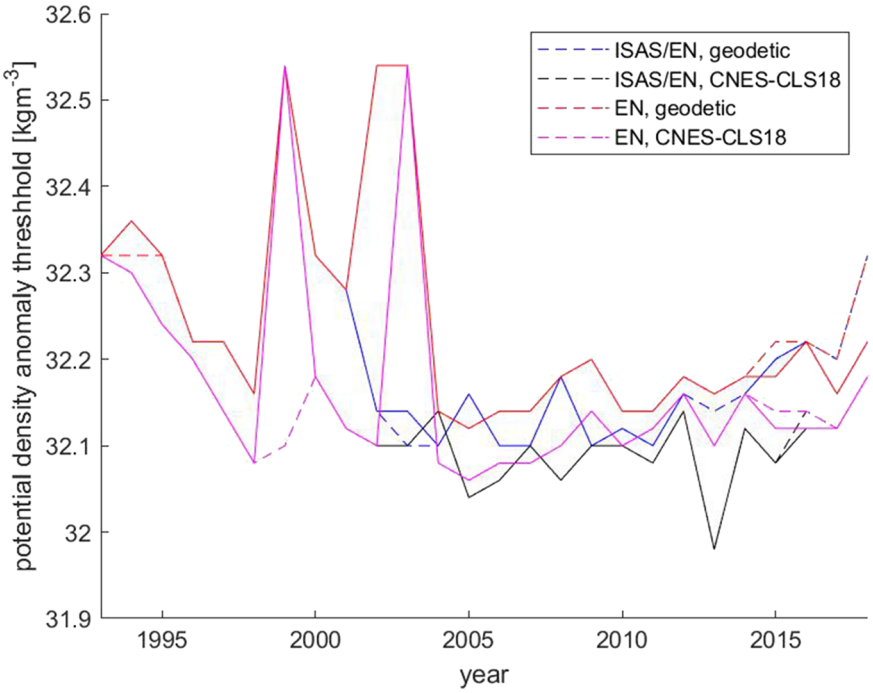

Figure 12. For the computation of the upper-limb transport MOC over the Greenland-Portugal section, the threshold potential density anomaly σ_{th} is displayed. σ_{th} defines the density level where integration of section-accumulated transports, which is started from the surface, maximizes. The applied hydrography (EN or combined ISAS/EN) and MDT model (CNES-CLS18 or geodetic) is indicated in the inset. For solid (dashed) lines geoid height trend is included (excluded) in dynamic topography computation.

For a closer view in the bottom panel of Figure 11, we subtracted the geoid height trend as obtained from our extended composite (see section 8.1) from the sterically corrected SLA. Outside of the North Atlantic, the spatial structure of positive and negative trend patches is hardly changed, though significant changes in amplitudes are found. Due to the strong negative geoid height trend south of Greenland, the low negative trend in sterically corrected SLA changes to an increase of approximately 1 mm a^{-1} close to he coast. As above for the surface circulation in the subpolar North Atlantic also investigations of the deep circulation and associated heat and salt transports based on altimetry data are affected by geoid height trends.

8.4. Overturning From Combining Altimetry With In Situ Hydrography

In section 8.2 we have already discussed the impact on estimating changes in the surface circulation of the Subpolar North Atlantic from altimetry when disregarding changes in geoid height. Performing the investigation on a coast-to-coast section and adding density information from hydrography allows to extend this analysis to temporal variability of the MOC of the Atlantic, which is a crucial element in climate research. Specifically with the increased availability of in situ hydrography from ARGO floats, the combination of in situ hydrography, altimetry, and (optionally) wind speed data/models becomes an alternative or complement to the elaborate and expensive section-based measurements from ship cruises or moored instruments. Specifically long-term trends are an important issue and this is where geoid height trends might essentially bias the results.

The section where MOC variability is investigated is defined as two connected geodetic lines, starting from Cape Farewell and ending at the coast of Portugal (see Figure 11, top) and is close to the OVIDE and FOUREX sections (see, e.g., Mercier et al. 2015). The methodology described in section 2.4 follows largely the methodology described by Mercier et al. (2015). To investigate both interannual to longer-term changes as well as seasonal variations, the computations here work either with annual or monthly climatological means for the period 1993–2018. To investigate the impact of the geoid height in comparison to uncertainties in other data sets, we compute an ensemble of MOC estimates by combining two MDT models (CNES-CLS18 and a geodetic MDT) with two hydrography databases (ISAS and EN4). Utilizing all possible combinations results

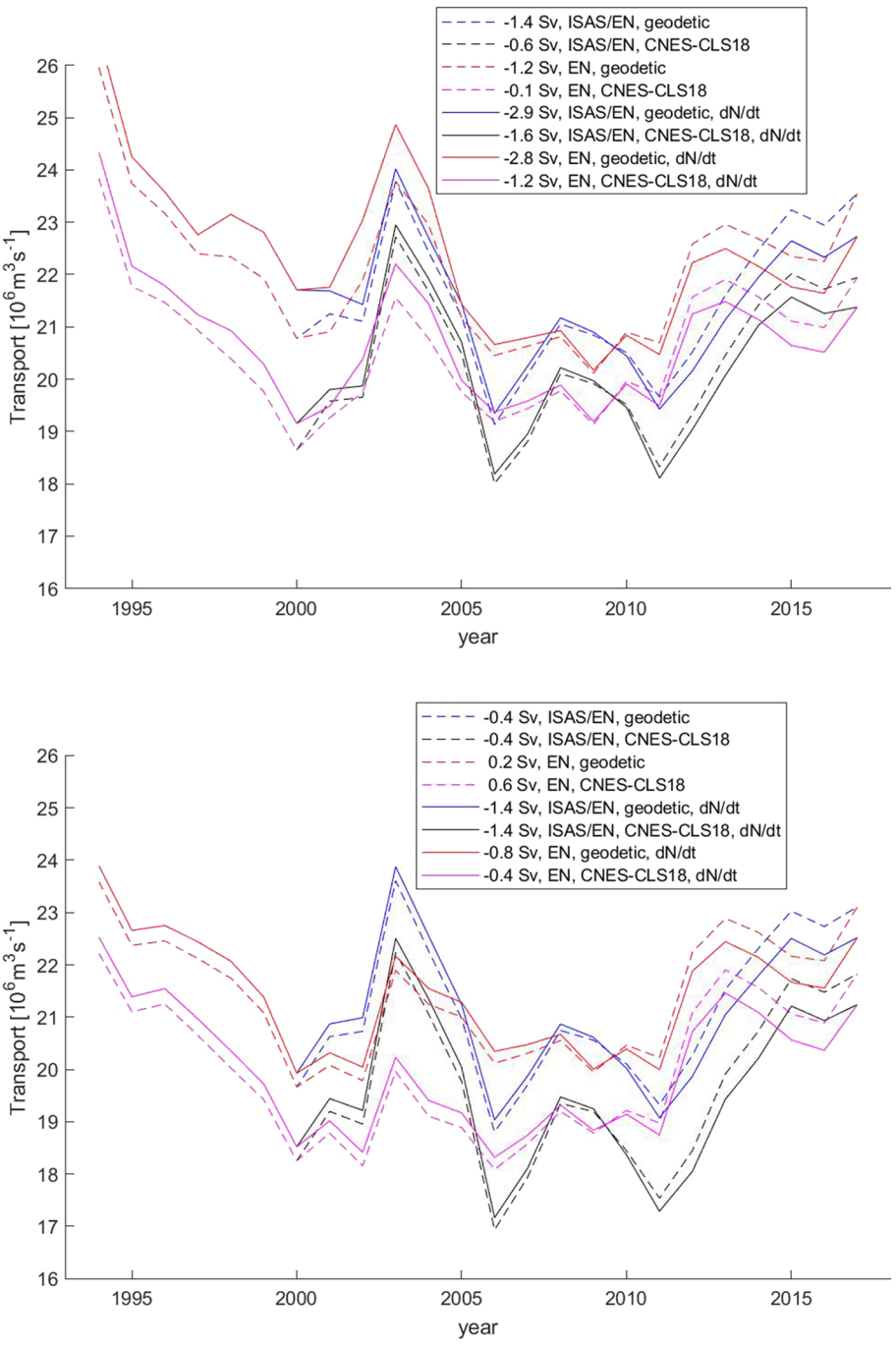

Figure 13. Running 3-year mean MOC for years 1994–2017. The change in MOC within the period, according to the linear trend, is provided in the inset, together with the applied hydrography (EN or combined ISAS/EN) and MDT model (CNES-CLS18 or geodetic). (Top) Integration is performed down to the threshhold potential density anomaly as shown in Figure 12. (bottom) Integration is always performed down to potential density anomaly $\sigma = 32.16 kg\,m^{-3}$.'

in an ensemble of four members. Since ISAS is only available for 14 years from 2002–2015, which is too short for our purpose, the years 1993–2001 and 2016–2018 are filled with data from EN4.

We found, however, a large variance for the threshold potential density that marks the lower bound of the upper branch of the MOC (see Figure 12). Those unrealistic variations are probably caused by mesoscale variability in SLA, where the corresponding steric effects cannot be resolved by the hydrography data base and will thus cause unrealistic geostrophic currents. We have thus, in a second ensemble, fixed the

threshold potential density to 32.16 kg m^{-3}, the value found by Mercier et al. (2015) for 1997–2010 based on measurements on the OVIDE and FOUREX sections.

Both ensembles were computed for both annual averages and monthly climatological means. Considering climatological means, the impact of seasonal geoid height changes is, however, less than 0.2 Sv (1 Sv = 10^6 m^3 s^{-1}) no matter which threshhold density or ensemble member is considered. We thus conclude that geoid variations are negligible for seasonal MOC variations on the section.

The results based on annual mean data are displayed in Figure 13 averaged to 3-year running means. For both ensembles and all members a decreasing MOC during the 1990s, a maximum around 2003, and a weak MOC between 2006–20011 is observed. This is generally close to the results of Mercier et al. (2015), though they found a strong MOC around 2010. Fixing the threshold potential density to 32.16 kg m^{-3} lowers the MOC on average by approximately 0.7 Sv, has some impact on the magnitude of extremes, and increases the linear trend for all ensemble members. Trends are lowered by at least 1.0 Sv $year^{-1}$ for every ensemble member. When not fixing the threshhold density, the mean trend is changed from −0.8 to −2.1 Sv $year^{-1}$ when geoid height changes are considered, while when fixing the threshhold, the trend changes from 0.0 to −1.0 Sv $year^{-1}$. Though given the small number of members (and the partly dependence of the data), a robust estimation of uncertainty of the MOC estimates can hardly be provided; it can be stated that the geoid height trend at least has a significant impact on the MOC trend that will increase with extended periods considered and an accelerated geoid height trend for Greenland in the future.

9. Conclusions

This paper discusses the weekly to interannual variations in geoid height as a whole and subdivided into the contributions from water mass cycling between the Earth system components (TWS and land ice, global atmosphere, and ocean mass), the atmospheric and ocean dynamics, and GIA.The analysis is performed on different time scales, and the regional patterns should allow investigators working with SLA or ODT to decide whether temporal variations in the geoid have to be considered significant in their study or are negligible.

Our main conclusions are as follows:

1. Submonthly geoid height variability over the ocean due to redistribution of atmospheric mass is everywhere small because of the IB effect (RMS below 2 mm), specifically away from the coast (below 1 mm).
2. Monthly geoid height variations are between 0.5 and 5 mm over the oceans. Larger RMS values are found only along the Greenland coast.
3. After subtraction of the annual mean, the monthly variations are predominantly caused by changes in TWS and atmospheric mass redistribution with only minor contributions from ocean dynamics (below 2 mm). These intraannual variations are generally well represented by a seasonal cycle defined as a trigonometric function.
4. For the geoid height trend over the period considered (2003–2011), only GIA and TWS changes play a role with the largest, negative, signals around Greenland and in the Pacific section of the Southern Ocean due to decreasing ice sheets and a positive signal south of the African continent.
5. Geoid height variations are usually not considered when altimetry data are applied to investigate changes in ocean dynamics. From our study this seems justified if short temporal (up to interannual) or spatial scales (up to 1,000 km or so) are considered. However, for the subpolar North Atlantic, due to the melt of the Greenland ice sheet, the associated strong geoid height trend is biasing long-term changes in surface and deep ocean currents based on (sterically corrected) altimetry data. A correction for the geoid height change is necessary in that region when investigating long-term changes in sea level based on altimetry data.

Data Availability Statement

The GRACE RL05 Mascon solution was downloaded online (https://grace.jpl.nasa.gov). The Ssalto/Duacs altimeter products were produced and distributed by the Copernicus Marine and Environment Monitoring Service (CMEMS) (http://www.marine.copernicus.eu). NCEP Reanalysis data are provided by the NOAA/OAR/ESRL PSD, Boulder, Colorado, USA, from their Web site (https://www.esrl.noaa.gov/psd/).

The EN.4.2.1 quality controlled ocean data are provided by the Met Office Hadley Centre for Climate Change (https://www.metoffice.gov.uk/hadobs/en4/download-en4-2-1.html). The ISAS-15 temperature and salinity gridded fields are obtained from SEANOE (SEA scieNtific Open data Edition; https://www.seanoe.org/data/00412/52367/). The aggregated Greenland Ice Sheet mass balance data from the IMBIE project were downloaded online (http://imbie.org). The computations of geoid height from GRACE AOD products and all necessary transformations between gridded data and spherical harmonic coefficients were performed with the GOCE User Toolbox (GUT), provided by the European Space Agency (ESA) and available online (https://earth.esa.int/web/guest/software-tools/gut/about-gut/overview). MDT-CNES-CLS was produced by CLS and distributed by Aviso+, with support from Cnes (https://www.aviso.altimetry.fr/).

Acknowledgments
Support for the research was partially provided by the German Science Foundation (DFG) under the priority program SPP 1889 ("Regional Sea Level Change and Society") and by the BMBF funded Verbundprojekt RACE (Regional Atlantic Circulation and Global Change). The study is a contribution to the Cluster of Excellence "Integrated Climate System Analysis and Prediction" (CliSAP) of the University of Hamburg, funded by the DFG. Thanks to two anonymous reviewers for their valuable comments and suggestions which helped greatly to improve the original manuscript. Open access funding enabled and organized by Projekt DEAL.

References

Andersen, O. B., Stenseng, L., Piccioni, G., & Knudsen, P. (2016). The DTU15 MSS (mean sea surface) and DTU15lat (lowest astronomical tide) reference surface. In *ESA Living planet symposium 2016*, Prague, Czech Republic.

Bruinsma, S. L., Först, C., Abrikosov, O., Lemoine, J.-M., Martyy, J.-C., Mulet, S., et al. (2014). ESA's satellite-only gravity field model via the direct approach based on all GOCE data. *Geophysical Research Letters*, *41*, 7508–7514. https://doi.org/10.1002/2014GL062045

Caron, L., Ivins, E. R., Larour, E., Adhikari, S., Nilsson, J., & Blewitt, G. (2018). GIA model statistics for GRACE hydrology, cryosphere and ocean science. *Geophysical Research Letters*, *45*, 2203–2212. https://doi.org/10.1002/2017GL076644

Chambers, D. P., & Willis, J. K. (2008). Analysis of large-scale ocean bottom pressure variability in the North Pacific. *Journal of Geophysical Research*, *113*, C11003. https://doi.org/10.1029/2008JC004930

Chao, B. F. (2003). Geodesy is not just for static measurements any more. *Eos Transactions of the American Geophysical Union*, *84*(16), 145–150.

Chen, J. L., Wilson, C. R., Tapley, B. D., Save, H., & Cretaux, J. F. (2017). Long-term and seasonal Caspian sea level change from satellite gravity and altimeter measurements. *Journal of Geophysical Research: Solid Earth*, *122*, 2274–2290. https://doi.org/10.1002/2016JB013595

Christodoulidis, D. (1979). Influence of the atmospheric masses on the gravitational field of the Earth. *Bulletin Gœodésique*, *53*, 61–77.

Dahle, C., Flechtner, F., Gruber, C., König, D., König, R., Michalak, G., & Neumayer, K.-H. (2013). GFZ GRACE Level-2 processing standards document for Level-2 product release 0005 (*Scientific Technical Report STR12/02 - Data*). Revised Edition.

Dayoub, N., Edwards, S. J., & Moore, P. (2012). The Gauss-Listing geopotential value W0 and its rate from altimetric mean sea level and GRACE. *Journal of Geodesy*, *86*(9), 681–694.

Dickey, J. O., et al. (1997). Satellite gravity and the geosphere. Washington, DC: National Academy.

Dobslaw, H., Flechtner, F., Bergmann-Wolf, I., Dahle, C., Dill, R., Esselborn, S., et al. (2013). Simulating high-frequency atmosphere-ocean mass variability for dealiasing of satellite gravity observations: AOD1B RL05. *Journal of Geophysical Research: Oceans*, *118*, 3704–3711. https://doi.org/10.1002/jgrc.20271

Ecker, E., & Mittermayer, E. (1969). Gravity correction for the influence of the atmosphere. *Bollettino di Geofisica Teorica e Applicata*, *11*(41), 70–80.

Flechtner, F., Dobslaw, H., & Fagiolini, E. (2015). AOD1B product description document for product release 05: GFZ German Research Center for Geosciences. https://www.gfz-potsdam.de/fileadmin/gfz/sec12/pdf/GRACE/AOD1B/AOD1B_20150423.pdf

Frederikse, T., Simon, K., Katsman, C. A., & Riva, R. (2017). The sea-level budget along the northwest atlantic coast: GIA, mass changes, and large-scale ocean dynamics. *Journal of Geophysical Research: Oceans*, *122*, 5486–5501. https://doi.org/10.1002/2017JC012699

Gaillard, F., Reynaud, T., v. Thierry, Kolodziejczyk, N., & Schuckmann, K. Von (2016). In-situ based reanalysis of the global ocean temperature and salinity with ISAS: Variability of the heat content and steric height. *Journal Of Climate*, *29*(4), 1305–1323.

Geruo, A., Wahr, J., & Zhong, S. (2012). Computations of the viscoelastic response of a 3-D compressible earth to surface loading: an application to glacial isostatic adjustment in antarctica and Canada. *Geophysical Journal International*, *192*(2), 557–572. https://doi.org/10.1093/gji/ggs030

Gilardoni, M., Reguzzoni, M., & Sampietro, D. (2016). GECO: A global gravity model by locally combining GOCE data and EGM2008. *Studia Geophysica et Geodaetica*, *60*, 228–247. https://doi.org/10.1007/s11200-015-1114-4

Good, S. A., Martin, M. J., & Rayner, N. A. (2013). EN4: quality controlled ocean temperature and salinity profiles and monthly objective analyses with uncertainty estimates. *Journal of Geophysical Research: Oceans*, *118*, 6704–6716. https://doi.org/10.1002/2013JC009067

Hatun, H., & Chafik, L. (2018). On the recent ambiguity of the north atlantic subpolar gyre index. *Journal of Geophysical Research: Oceans*, *123*, 5072–5076. https://doi.org/10.1029/2018JC014101

Hofmann-Wellenhof, B., & Moritz, H. (2006). *Physical Geodesy* (2nd ed.). Wien: Springer.

Jin, S., Zhang, T. Y., & Zou., F. (2017). Glacial density and GIA in alaska estimated from ICESat, GPS and GRACE measurements. *Journal of Geophysical Research: Earth Surface*, *122*, 76–90. https://doi.org/10.1002/2016JF003926

Kalnay, Kanamitsu, M., Kistler, R., Collins, W., Deaven, D., Gandin, L., et al. (1996). The NCEP/NCAR 40-year reanalysis project. *Bulletin of the American Meteorological Society*, *77*, 437–470.

Köhl, A. (2015). Evaluation of the GECCO2 ocean synthesis: Transports of volume, heat and freshwater in the atlantic. *Quarterly Journal of the Royal Meteorological Society*, *141*(686), 166–181. https://doi.org/10.1002/qj.2347

Kolodziejczyk, N., Prigent-Mazella, A., & Gaillard, F. (2017). ISAS-15 temperature and salinity gridded fields. SEANOE. https://doi.org/10.17882/52367

Mercier, H., Lherminier, P., Sarafanov, A., Gaillard, F., Daniault, N., Desbruyére, D., et al. (2015). Variability of the meridional overturning circulation at the Greenland-Portugal OVIDE section from 1993 to 2010. *Progress in Oceanography*, *132*, 250–261.

Moore, P., Zhang, Q., & Alothman, A. (2005). Annual and semiannual variations of the Earth's gravitational field from satellite laser ranging and CHAMP. *Journal of Geophysical Research*, *110*, B06401. https://doi.org/10.1029/2004JB003448

Moore, P., Zhang, Q., & Alothman, A. (2006). Recent results on modelling the spatial and temporal structure of the Earth's gravity field. *Philosophical Transactions of the Royal Society A-Mathematical,Physical and Engineering Sciences*, *364*(1841), 1009–1026.

Nerem, R. S., Eanes, R. J., Thompson, P. F., & Chen, J. L. (2000). Observations of annual variations of the Earth's gravitational field using satellite laser ranging and geophysical models. *Geophysical Research Letters*, *27*(12), 1783–1786. https://doi.org/10.1029/1999GL008440

Rio, M. H., Mulet, S., & Picot, N. (2014). Beyond GOCE for the ocean circulation estimate: Synergetic use of altimetry, gravimetry, and in situ data provides new insight into geostrophic and ekman currents. *Geophysical Research Letters*, *41*, 8918–8925. https://doi.org/10.1002/2014GL061773

Rummel, R., Balmino, G., Johannessen, J., Visser, P., & Woodworth, P. (2002). Dedicated gravity field missions—Principles and aims. *Journal of Geodynamics*, *33*(1–2), 3–20.

Rummel, R., & Rapp, R. H. (1976). The influence of the atmosphere on geoid and potential coefficient determinations from gravity data. *Journal of Geophysical Research*, *81*, 5639–5642.

Siegismund, F. (2020). A spectrally consistent globally defined geodetic mean dynamic ocean topography. *Journal of Geophysical Research: Oceans*, *125*, e2019JC016031. https://doi.org/10.1029/2019JC016031

Slangen, A. B. A., Adloff, F., Jevrejeva, S., Leclercq, P. W., Marzeion, B., Wada, Y., & Winkelmann, R. (2017). A review of recent updates of sea-level projections at global and regional scales. *Surveys in Geophysics*, *38*(1), 385–406.

Stammer, D., Wunsch, C., & Ponte, R. (2000). De-Aliasing of global high frequency barotropic motions in altimeter observations. *Geophysical Research Letters*, *27*, 1175–1178.

Tamisiea, M. E., Hill, E. M., Ponte, R. M., Davis, J. L., Velicogna, I., & Vinogradova, N. T. (2010). Impact of self-attraction and loading on the annual cycle in sea level. *Journal of Geophysical Research*, *115*, C07004. https://doi.org/10.1029/2009JC005687

Tapley, B. D., Bettadpur, S., Watkins, M. M., & Reigber, C. (2004). The gravity recovery and climate experiment: Mission overview and early results. *Geophysical Research Letters*, *31*, L09607. https://doi.org/10.1029/2004GL019920

Tapley, B. D., Watkins, M. M., Flechtner, F., Reigber, C., Bettadpur, S., Rodell, M., et al. (2019). Contributions of GRACE to understanding climate change. *Nature Climate Change*, *5*(5), 358–369. https://doi.org/10.1038/s41558-019-0456-2

Team, T. I. (2020). Mass balance of the Greenland ice sheet from 1992 to 2018. *Nature*, *579*, 233–239. https://doi.org/10.1038/s41586-019-1855-2

Vinogradova, N. T., Ponte, R. M., Tamisiea, M. E., Davis, J. L., & Hill, E. M. (2010). Effects of self-attraction and loading on annual variations of ocean bottom pressure. *Journal of Geophysical Research*, *115*, C06025. https://doi.org/10.1029/2009JC005783

Vinogradova, N. T., Ponte, R. M., Tamisiea, M. E., Quinn, K. J., & Hill, E. M. (2011). Self-attraction and loading effects on ocean mass redistribution at monthly and longer time scales. *Journal of Geophysical Research*, *116*, C08041. https://doi.org/10.1029/2011JC007037

Wahr, J., Molenaar, M., & Bryan, F. (1998). Time variability of the Earth's gravity field: Hydrological and oceanic effects and their possible detection using GRACE. *Journal of Geophysical Research*, *103*(B12), 30,205–30,229.

Watkins, M. M., Wiese, D. N., Yuan, D.-N., Boening, C., & Landerer, F. W. (2015). Improved methods for observing Earth's time variable mass distribution with GRACE using spherical cap mascons. *Journal of Geophysical Research: Solid Earth*, *120*, 2648–2671. https://doi.org/10.1002/2014JB011547

Wiese, D. N., Landerer, F. W., & Watkins, M. M. (2016). Quantifying and reducing leakage errors in the JPL RL05M GRACE mascon solution. *Water Resources Research*, *52*, 7490–7502. https://doi.org/10.1002/2016WR019344

Wiese, D. N., Yuan, D.-N., Boening, C., Landerer, F. W., & Watkins, M. M. (2015). JPL GRACE mascon ocean, ice, and hydrology equivalent water height JPL RL05M.1. ver. 1. In *PO.DAAC, Calif.* https://doi.org/10.5067/TEMSC-OCL05